

Teleconnection Mechanisms For Tropical Pacific Descent Anomalies During El Niño

Hui Su and J. David Neelin

June 18, 2002

Department of Atmospheric Sciences
Institute of Geophysics and Planetary Physics
University of California, Los Angeles

Revised for *Journal of the Atmospheric Sciences*

Corresponding author address:

J. David Neelin

Department of Atmospheric Sciences

University of California at Los Angeles

Los Angeles, CA 90095-1565

Internet: neelin@atmos.ucla.edu

Phone: (310) 206-3734

Fax: (310) 206-5219

Abstract

Teleconnection mechanisms in relative descent zones are examined using the quasi-equilibrium tropical circulation model (QTCM). The regions of anomalous descent neighboring the warm sea surface temperature (SST) anomalies in the eastern and central Pacific Ocean during the 1997-1998 El Niño are used as an example and results are verified for three other El Niño warm events (1982, 1987, 1991). By analyzing the moisture and moist static energy budgets over these regions, it is found that the physical processes responsible for the descent anomalies are different for each region. Anomalous dry advection is the dominant mechanism for the reduced precipitation to the north of the El Niño warm region. On the other hand, the relative descent to the south of the El Niño warm SSTs is caused by reduced surface wind speed and reduced air-sea contrast and resulting weaker than normal evaporation. Budget analysis based on the National Aeronautics and Space Administration Seasonal-to-Interannual Prediction Project atmospheric general circulation model simulations is consistent with the QTCM results. Radiative cooling associated with the warming of tropospheric temperature is relatively small, on the order of a few Wm^{-2} . The traditional assumption that compensating subsidence is caused by radiative cooling due to increased tropospheric temperature thus does not apply in this context. An experiment to test this by suppressing the radiative cooling due to temperature anomalies showed little impact on the descent anomalies. Thus radiative cooling is not even an initiator of descent anomalies. Instead, relative descent tends to occur in particular regions where other larger cooling or drying tendencies act. Reductions in convective heating and cloud radiative heating behave like a reduction in effective static stability, enhancing the descent anomalies. The complexity of the mechanisms for the descent anomalies may be responsible for the difficulty of descent zone simulation and forecast in general circulation models.

1 Introduction

Teleconnections from tropical sea surface temperature (SST) anomalies or convective heating are among the most important interannual climate variability (Wallace and Gutzler 1981; Wallace et al. 1998; Trenberth et al. 1998). Considerable theory has been developed for tropical to midlatitude teleconnection (Simmons et al. 1983; Held et al. 1989; Hoskins and Karoly 1981; Hoerling and Ting 1994; Straus and Shukla 1997). There has also been considerable work on tropical wave dynamics in producing remote response to a heat source (Matsuno 1966; Webster 1972; Gill 1980; Salby and Garcia 1987), including the effects of zonally varying basic state (Webster and Chang 1988). However, these studies treated moist convection as an external heating source to the total dynamical system and did not consider the complex interaction between convection and large-scale motions. Cloud-radiative feedback and land-surface processes were also omitted. We address tropical teleconnections with moist dynamics in a series of papers. Su et al. (2001, hereafter SNC) described the responses to SST anomalies in different parts of tropical oceans. The current paper focuses on the relative contribution of each physical process in producing the descent anomalies in the neighboring regions of warm SST anomalies during El Niño.

The broad structure of El Niño forced descent anomalies has been captured by many general circulation model (GCM) simulations (e.g. Lau 1985; Barnett et al. 1994; Kumar and Hoerling 1998; Mechoso et al. 1987; Farrara et al. 2000; Barnston et al. 1999; Trenberth et al. 1998;

Goddard and Graham 1999; Latif et al. 1999; Saravanan and Chang 2000; Soden 2000), although detailed features vary from model to model. However, none of the GCM studies examined the physical mechanisms responsible for the descent anomalies forced by the warm SST anomalies in El Niño events. In particular, the relative importance of each physical process in determining the El Niño related negative precipitation anomalies is not well documented.

The regions of descent anomalies of interest here are fundamentally different from the absolute descent regions, for example, over the Sahara desert, in that they are within convective zones and experiencing absolute rising motions. The negative precipitation anomalies result from shifts of convective zones. Hence, the mechanisms for the formation of descent anomalies here could be quite different from theories for absolute descent regions. Because convection still occurs, moist dynamics and cloud-radiation as well as land-surface processes may all come into play and complicate the mechanisms for descent anomalies. We refer to the areas of negative precipitation anomalies in response to the warm SST forcings in the main El Niño region as areas of “relative subsidence” or “descent anomalies”. Comparison between the negative precipitation anomaly regions and anomalous descent regions on seasonal time scales shows especially good correlation between the two fields in both observations and model simulations. We thus use the terms “descent anomalies”, “relative descent” or “negative precipitation anomalies” interchangeably, to refer to the different aspects of the same climate feature.

Traditional theory for the response to a localized heat source did not focus on the descent regions (e.g. Charney 1959; Matsuno 1966; Webster 1972; Gill 1980). A tacit assumption was made that radiative cooling provided the descent mechanism. To summarize explicitly the mechanisms in this “traditional view”: wave dynamics spreads the warming from a convective region to a broad area. Away from the heat source, longwave cooling associated with the anomalous warm tropospheric temperature induces descent anomalies, with adiabatic warming balancing the radiative cooling. From this point of view, one would expect that compensating descent anomalies would be strongly tied to tropospheric temperature anomalies, which are relatively uniform over the whole tropical band (Wallace et al. 1998; SNC). However, descent anomalies are relatively localized (Ropelewski and Halpert 1987; Soden 2000; SNC) compared to tropospheric temperature anomalies. The two do not appear to be related in a simple manner. Mechanisms affecting subtropical absolute descent zones have been examined by Rodwell and Hoskins (1996), in which the Rossby-wave pattern induced by the Asian monsoon contributes to desertification to the west. In contrast, the physical processes for the relative descent within the convective zones have not been explored.

During El Niño warm events, increased precipitation occurs over the central and eastern Pacific associated with the warm SST anomalies. Surrounding the positive precipitation anomalies, negative precipitation anomalies are observed to the north and south, and in the western Pacific. As discussed in SNC, the reduced precipitation regions to the north and south of the main ENSO warm area are mostly a remote response to positive SST anomalies. This makes it appropriate to study the mechanisms for descent anomalies in these regions as a reference for general teleconnection theories. We have conducted experiments for a number of El Niño years. The MSE budget analysis produces consistent results for all major warm events. We thus focus on the 1997-1998 El Niño event, and present results for other years using composite analysis.

The quasi-equilibrium tropical circulation model (QTCM) is used, forced by observed positive SST anomalies added onto the climatological SST in the tropical Pacific Ocean. SNC presents a series of model simulations with SST anomalies specified in subregions of tropical oceans during

the 1997-1998 El Niño event. It is found that the QTCM forced with observed SSTs simulates well major El Niño related variability in precipitation, temperature and wind fields. Our results are generally similar to corresponding GCM studies (Frederiksen et al. 2001; Farrara et al. 2000). The QTCM is well-suited for diagnosis of mechanisms in such ENSO response studies. Not only is it computationally fast, but also is amenable to budget analysis. For example, the moist static energy (MSE) equation follows the atmospheric primitive equation but takes a simple form in the model system. With the results from such an intermediate complexity atmospheric circulation model, we wish to shed light on the subject and provide an example that may assist GCM analysis.

The paper is organized as follows: section 2 describes the model physics and the design of experiments. In section 3, the horizontal distribution of simulated vertical motions, precipitation, tropospheric temperature and wind anomalies as well as outgoing longwave radiation (OLR) anomalies for JFM 1998 are presented and compared to observations. Detailed moisture budget and moist static energy budget analyses are given in section 4, with focus on three regions in the tropical Pacific Ocean. For comparison, similar budget analysis is applied to the model simulations from the National Aeronautics and Space Administration (NASA) Seasonal-to-Interannual Prediction Project (NSIPP) atmospheric general circulation model (AGCM). Results are shown in section 5. Section 6 describes the composite MSE budget results for three other major El Niño events. Motivated by the budget analysis, we design several mechanism-testing experiments to explore the role of radiative cooling versus other “cooling” mechanisms in determining the relative descent in response to warm SST anomalies. Section 7 presents the results of these experiments. The concluding section 8 first summarizes the model results, then a revised theory for teleconnection mechanisms in relative descent zones is proposed.

2 The QTCM and experiment design

We use the quasi-equilibrium tropical circulation model (QTCM) version 2.2 to conduct experiments forced by specified SST distribution based on observed SST during the 1997-1998 El Niño. The model formulation and general performance are described in Neelin and Zeng (2000) and Zeng et al. (2000). In short, this model utilizes simplifications based on quasi-equilibrium moist convective closure and includes nonlinear advection of temperature and moisture, Betts-Miller convective adjustment and weakly nonlinear cloud radiative feedback as well as a simple interactive land model. The standard v2.2 has only deep convective cloud and cirrostratus/cirrocumulus (CsCc) interactive in radiation. To achieve a better representation of cloud-radiative feedback in the tropics on large spatial scale and time scales longer than a month, the fraction of cirrus cloud is made proportional to the deep convective cloud (cirrus:deep convective cloud = 1:1, see Fig. 5.15 in Chou 1997). The effect of other cloud types (altostratus/altocumulus and cumulus/stratocumulus) in this El Niño event is considered to be half of the cirrus contribution in total radiative heating rate (based on calculations using the International Satellite Cloud Climatology Project (ISCCP) observed cloud fractions during the 1986-1987 El Niño). For the 1997-1998 El Niño, the model was able to reproduce major El Niño signals in precipitation, temperature, moisture and wind fields as shown in SNC.

In this paper, in order to investigate the mechanisms for relative descent in response to El Niño warm SST forcing, we focus on the simulation called “POSPAC” as in SNC. The “POSPAC” run includes only positive SST anomalies in the tropical Pacific Ocean observed during January-March

1998. The design of experiments for the current study is similar to that of SNC, in that ensemble means of ten simulations with slightly different initial conditions are constructed and compared to those of a similar ensemble of control runs (called “CLIM”), in which climatological SST is used over the whole model domain (0° - 360° , 60°S - 60°N). The anomalies are then defined as the difference between the ensemble mean of ten “POSPAC” runs and the ensemble mean of ten “CLIM” runs. The ten initial conditions are obtained from a ten year integration using seasonal SST. The thermodynamic and dynamical variables at the end of each year are saved as one of the initial conditions for ensemble integrations. The transient variability between members of the ensemble runs is very small compared to El Niño-related teleconnection signals.

Besides the two primary model runs, we also designed a set of experiments to test the importance of particular mechanisms for descent anomalies. In experiments CLIMRAD.NORTH and CLIMRAD.SOUTH, we suppress the radiative cooling associated with anomalous warming of the atmosphere and use only climatological radiative heating rate due to temperature in target regions (to the north and south of the main El Niño warm SSTs, respectively). Comparing them to the POSPAC run, the effect of anomalous radiative cooling due to atmospheric warming in creating the descent anomalies can be evaluated. In another experiment named ADV.NORTH, the advection of temperature and moisture (plus horizontal diffusion of temperature and moisture) are held at their climatological values to the north of the El Niño warming. In experiment SFLUX.SOUTH, the surface latent and sensible heat flux anomalies are suppressed in a region to the south of the El Niño warming area. The roles of advection and surface flux anomalies in producing the anomalous descent in particular regions are then tested. Ensemble simulations with the same initial conditions as the POSPAC and CLIM runs are conducted.

3 Simulated anomalies in the POSPAC run

As presented in SNC, the QTCM reproduces major El Niño related variability in precipitation, tropospheric temperature and wind anomalies during the 1997-1998 El Niño. Although the detailed patterns of response to El Niño SSTs vary slightly with different model versions, the general features of simulations are robust. Because we focus on “descent anomalies”, Fig. 1 shows 500 hPa vertical pressure velocity ω anomalies during JFM 1998 from the National Centers for Environmental Prediction (NCEP)/National Center for Atmospheric Research (NCAR) reanalysis (Kalnay et al. 1996), the QTCM simulation with observed global (60°S - 60°N) SST, and the POSPAC run as described in section 2. Compared to the NCEP/NCAR reanalysis (Fig. 1a), the modeled ω anomalies are satisfactory (Fig. 1b), especially within tropics (25°S - 25°N), although the overall amplitude is smaller. In the POSPAC run, the anomalous rising motion coincides with warm SST anomalies (see SNC Fig. 1b or Fig. 5c in this paper). Strong descent anomalies are concentrated in the Pacific Ocean, and in the eastern equatorial South America. The missing downward anomalies in the western Pacific and upward anomalies in the Indian Ocean are mostly contributed by local SST anomalies (see SNC), which are not included in the POSPAC run.

Figure 2 displays model-simulated precipitation anomalies, tropospheric temperature anomalies averaged for 850–200 hPa superimposed with 850 hPa wind anomalies, and outgoing longwave radiation (OLR) anomalies in the POSPAC run. The precipitation anomalies (Fig. 2a) are consistent with ω anomalies in Fig. 1c, i.e., the anomalous rising motions are co-located with positive

precipitation anomalies, and the descent anomalies correspond to negative precipitation anomalies. Hence, we use “descent anomalies” and “negative precipitation anomalies”, interchangeably, to refer to the same regions in the Pacific Ocean. The observed precipitation anomalies during JFM 1998 are shown in SNC (Fig. 2b), thus not repeated here. Similar to observations, relatively strong negative precipitation anomalies are adjacent to the increased precipitation areas in the eastern and central Pacific. The anomalies in northeast South America, central Australia and south central Africa are also evident (Fig. 2a).

Tropospheric averaged (850 hPa–200 hPa) temperature has a broad warming over the entire tropical band (Fig. 2b). The shape of tropospheric temperature anomalies resembles the classic wave response to a given localized heat source (Gill 1980), while the temperature anomalies are less symmetric about the equator than observations. An excessive local warm maxima over the western equatorial South America may be due to wave interaction with land-surface processes or with the zonally asymmetric basic state. The wind anomaly is associated with the anomalous temperature gradient by baroclinic dynamics and likewise spreads over a large region. As stressed in SNC, it appears that the scale of teleconnections in precipitation anomalies tends to be smaller than the scale of teleconnections in tropospheric temperature and wind anomalies.

Model-produced OLR anomalies are closely related to the precipitation anomalies, albeit broader to the north of main El Niño warm area (Fig. 2c). The magnitude of OLR anomalies is smaller than observed (e.g., the data from the National Oceanic and Atmospheric Administration Climate Diagnostics Center). It may be partly due to the smaller amplitude of precipitation anomalies generated in the model, thus producing a smaller cloud fraction, and may also partly result from the simplified radiative scheme.

4 Moisture and Moist Static Energy Budget Analysis

We focus on the mechanisms responsible for descent anomalies to the north and south of the main ENSO warm region in the tropical Pacific Ocean. The relative importance of each physical process in creating the precipitation anomalies over different regions is sought. The moisture and moist static energy budgets for each region are analyzed.

4.1 Formulation

The nonlinear primitive equations for temperature and moisture, when vertically integrated, take the following form

$$\partial_t \widehat{T} + \widehat{\mathcal{D}}_T T + \omega \widehat{\partial}_p s = \langle Q_c \rangle + (g/p_T)(F_{rad} + H) \quad (1)$$

$$\partial_t \widehat{q} + \widehat{\mathcal{D}}_q q + \omega \widehat{\partial}_p q = \langle Q_q \rangle + (g/p_T)E, \quad (2)$$

where both T and q are in energy units (Wm^{-2}) with C_p and L absorbed respectively and $s = T + \phi$ is the dry static energy, with ϕ the geopotential. The operators \mathcal{D}_T and \mathcal{D}_q include horizontal advection and horizontal diffusion terms. We use

$$\mathcal{D}_T = \mathcal{D}_q = \mathbf{v} \cdot \nabla - K_H \nabla^2. \quad (3)$$

The net radiative flux into the column is $F_{rad} = S_t^\downarrow - S_t^\uparrow - S_s^\downarrow + S_s^\uparrow - R_t^\uparrow - R_s^\downarrow + R_s^\uparrow$, where the upward and downward longwave radiative fluxes R_t^\uparrow , R_s^\downarrow and shortwave radiative fluxes S_t^\uparrow , S_s^\downarrow are functions of temperature, moisture and cloudiness in the column, signed in the direction of the flux. The surface sensible and latent heat fluxes are H and E , respectively. The convective heating and moisture sink are Q_c and Q_q , which satisfy the energy constraint over the air column

$$-\langle Q_q \rangle = \langle Q_c \rangle = (g/p_T)P \quad (4)$$

where P stands for precipitation (in Wm^{-2}).

In (1) and (2), $\widehat{(\)}$ or $\langle \ \rangle$ denotes vertical averaging over the troposphere, as defined in (5), with convective heating assumed confined below the tropopause.

$$\widehat{X} = \langle X \rangle = p_T^{-1} \int_{p_{rt}}^{p_{rs}} X dp \quad (5)$$

where $p_T = p_{rs} - p_{rt}$ is the constant reference pressure depth of the troposphere.

Combining (1) and (2), we obtain the vertically integrated moist static energy equation

$$\partial_t(\widehat{T} + \widehat{q}) + \widehat{\mathcal{D}_T T} + \widehat{\mathcal{D}_q q} + \omega \widehat{\partial_p h} = (g/p_T)(F_{rad} + E + H) \quad (6)$$

where the moist static energy is $h = s + q$. In the moist static energy equation, the column-averaged convective heating cancels the moisture sink. The large canceling terms that occur in the individual temperature and moisture equations are thus avoided.

Utilizing constraints placed on the flow by quasi-equilibrium convective closures, Neelin and Zeng (2000) derived a simple model system with tailored basis functions, the so-called quasi-equilibrium tropical circulation model (QTCM). In the model,

$$\omega \widehat{\partial_p s} = M_{S1} \nabla \cdot \mathbf{v}_1 \quad (7)$$

$$\omega \widehat{\partial_p q} = -M_{q1} \nabla \cdot \mathbf{v}_1 \quad (8)$$

$$\omega \widehat{\partial_p h} = M_1 \nabla \cdot \mathbf{v}_1 \quad (9)$$

where \mathbf{v}_1 is the wind component associated with baroclinic structure, and

$$M_1 = M_{S1} - M_{q1}. \quad (10)$$

Two new quantities associated with vertical stratification and stability emerge: M_{S1} and M_{q1} . As elaborated in Neelin and Zeng (2000), M_{S1} is the ‘‘gross dry stability’’ associated with the baroclinic wind convergence. M_{q1} is the ‘‘gross moisture stratification’’ arising from the vertical integral of moisture convergence associated with the baroclinic wind. Combining M_{S1} and M_{q1} , the ‘‘gross moist stability’’, $M_1 = M_{S1} - M_{q1}$, is an important stability parameter for moist convective regions. It gives the net thermal stratification resulting from the cancelling effect of adiabatic cooling and diabatic heating in convective zones (see Neelin 1997; Yu et al. 1998). It is generally substantially smaller than both M_{S1} and M_{q1} .

Considering the anomalies associated with ENSO warm SST forcing, we subtract the ensemble mean of each term in (2) and (6) for the control run with climatological SST from the ensemble

mean for the POSPAC run and average over JFM 1998, then obtain the equations for precipitation anomalies and moist static energy anomalies:

$$P' = (p_T/g)[(M_{q1}\nabla\cdot\mathbf{v}_1)' - \widehat{\mathcal{D}}_q q'] + E' \quad (11)$$

and

$$\widehat{\mathcal{D}}_T T' + \widehat{\mathcal{D}}_q q' + (M_1\nabla\cdot\mathbf{v}_1)' = (g/p_T)F_{rad}' + (g/p_T)E' + (g/p_T)H' \quad (12)$$

where ()' denotes the difference between the POSPAC and CLIM runs. It includes contributions from transient variability. In the QTCM, the radiative fluxes at the top of atmosphere and surface are computed using a weakly nonlinear radiation scheme depending on temperature, moisture, surface temperature and cloud fraction changes (Chou and Neelin 1996; Zeng et al. 2000). The F_{rad}' can be approximated as

$$F_{rad}' \approx \epsilon_T T_1' + \epsilon_q q_1' + \epsilon_{T_s} T_s' + CRF' \quad (13)$$

where ϵ_T , ϵ_q , and ϵ_{T_s} are the coefficients for radiative heating rate in the air column per unit change in the projection coefficients of temperature and moisture, and surface temperature change. CRF' represents the radiative heating rate due to cloud fraction change. In our model, only deep convective cloud, CsCc and cirrus cloud are interactive in dynamic feedbacks, while other cloud types are prescribed with climatological cloud distribution. Furthermore, the cloud fractions of interactive cloud types are linearly dependent on the amount of precipitation. Thus, cloud radiative forcing anomalies, CRF' , can be regarded as a feedback term, proportional to the precipitation anomalies:

$$CRF' \approx CP' \quad (14)$$

where C is a combined cloud radiative feedback parameter. When computed from the QTCM cloud radiative parameters, $C \approx 0.12$ in version 2.2 of the QTCM. Note that C includes only direct atmospheric heating effects (mostly longwave) and not cloud impacts on surface radiation since we are using fixed SST boundary conditions.

Using (14), (11) and (13), we can rewrite the moist static energy anomaly equation (12) as (horizontal diffusion neglected)

$$(M_{eff}\nabla\cdot\mathbf{v}_1)' = -\langle\mathbf{v}\cdot\nabla T\rangle' - (1+C)\langle\mathbf{v}\cdot\nabla q\rangle' + (g/p_T)(\epsilon_T T_1' + \epsilon_q q_1' + \epsilon_{T_s} T_s' + (1+C)E' + H') \quad (15)$$

where an ‘‘effective gross moist stability’’ arises,

$$M_{eff} = M_{S1} - (1+C)M_{q1}. \quad (16)$$

We note that the cloud-radiative feedback parameter (C) effectively decreases moist static stability, because the radiative warming (cooling) associated with increased (decreased) deep convective clouds opposes adiabatic cooling (warming) in the ascent (descent) regions. It also slightly modifies the weighting of moisture advection and evaporation in the moist static energy budget. We have placed all terms except the effective MSE divergence on the r.h.s. of (15) because in tropical dynamics, the divergence tends to respond very locally to forcing, whereas each of the other terms can mediate non-local response to the ENSO positive heating region. We thus begin the analysis by discussing the terms on the r.h.s. The non-local mechanisms are sought once the important terms are identified.

4.2 Moisture budget analysis results

Figure 3 shows the horizontal distribution of baroclinic wind convergence weighted by M_{q1} (Fig. 3a), moisture advection (Fig. 3b) and evaporation anomalies (Fig. 3c) produced in the model for JFM 1998. Only the Pacific region of the model domain is shown ($150^{\circ}\text{E} - 60^{\circ}\text{W}$, $30^{\circ}\text{S} - 30^{\circ}\text{N}$). Note that $(M_{q1}\nabla\cdot\mathbf{v}_1)'$ has a positive sign for net convergence of moisture into the column and vice versa. Moist advection $-\langle\mathbf{v}\cdot\nabla q\rangle'$ into the column would be positive and dry advection is negative in Fig. 3b. We outline three target regions in dark lines, denoted as ENSO WET (I), NORTH DRY (II) and SOUTH DRY (III) regions. The choice of boundary for the ENSO WET region is based on the 1 mm/day contour of precipitation anomalies. It tends to coincide with warm SST anomalies. Similarly, the boundaries for the NORTH DRY and SOUTH DRY regions are based on -1 mm/day contour of precipitation anomalies (see Fig. 2a). It is clear that convergent flow contributes most to the increased precipitation in the ENSO WET region (Fig. 3a). In the NORTH DRY and SOUTH DRY regions, divergent flow dominates and has similar pattern to the precipitation anomalies. In Fig. 3b, anomalous dry advection of moisture provides substantial drying to the NORTH DRY region. In other parts of the tropical Pacific, the anomalies of moisture advection are generally small.

On the other hand, evaporation strongly increases over the regions of warm SST anomalies. Its magnitude is about one quarter to one third of the anomalous moisture convergence (Fig. 3c). To the northwest, west and south of the main El Niño region evaporation decreases, which would contribute to the reduced precipitation in these areas. Over the SOUTH DRY region, the reduction of evaporation appears to be an important drying mechanism in addition to the significant drying due to moisture divergence. However, in most of the NORTH DRY region, east of 135°W , evaporation anomalies are noticeably positive, which would tend to counteract the drying effect of moisture divergence and moisture advection.

Averaged precipitation, moisture convergence, moisture advection and evaporation anomalies for each of the three target regions are summarized in Table 1. For the ENSO WET region, about 80% of the total averaged positive precipitation anomalies are contributed by convergent flow. Increased evaporation adds about 20%. Moisture advection anomalies are minimal, about 2 Wm^{-2} , which is comparable to the budget residuals (including diffusion, and truncation errors, etc).

In the NORTH DRY region, out of the 70.2 Wm^{-2} precipitation deficit, moisture divergence accounts for 75%. The second largest contribution to the negative precipitation anomalies comes from advection of moisture. It amounts to a drying tendency of 13.3 Wm^{-2} (about 19%). Averaged evaporation anomalies are small in the NORTH DRY region, less than 1 Wm^{-2} and tend to counteract the drying effect of other two terms.

For the SOUTH DRY region, 41 Wm^{-2} negative precipitation anomalies result mostly from moisture divergence and reduction of evaporation. They contribute approximately 30 Wm^{-2} (73%) and 8 Wm^{-2} (19%) to the averaged negative precipitation anomalies, respectively. Anomalous advection of moisture is only -1.3 Wm^{-2} (3%).

From the moisture budget in Table 1, we note that precipitation and moisture convergence are the two largest terms in the moisture budget. The seeming balance between precipitation anomalies and moisture divergence camouflages the relative importance of other drying mechanisms—advection of moisture and evaporation, etc. It is worth noting that moisture convergence is in fact a “feedback” not a “cause” in the chain of moist convective response to warm SST forcing.

The feedback among convective heating, adiabatic cooling and moisture convergence determines the convergence as a response to other physical processes. This response is most easily analyzed by turning to the moist static energy equation in which the substantial cancelation between moisture convergence and adiabatic cooling associated with rising motions is taken into account by the gross moist stability, thus the role of other physical processes in determining the convergence (and thus the moisture convergence) is more evident.

4.3 Moist static energy budget analysis results

The moist static energy equation is a useful tool for analyzing model thermodynamic balance because it combines the physical processes affecting temperature and moisture. As in Fig. 3, Figs. 4–7 are for anomalies for the ensemble of POSPAC runs relative to the CLIM ensemble. Figures 4 and 5 show the leading terms in (15), except advection of moisture and evaporation, because they have already appeared in Fig. 3. Their contributions in the moist static energy budget (with cloud-radiation feedback absorbed) differ from that in the moisture budget only by a small factor of 1.2. In Fig. 4, the term $(M_{\text{eff}} \nabla \cdot \mathbf{v}_1)' = ((M_{S1} - (1+C)M_{q1}) \nabla \cdot \mathbf{v}_1)'$ is the convergence with cloud-radiative effects absorbed as a feedback. Figure 4b displays the cloud-radiative effect itself. Anomalous advection of temperature is shown in Fig. 4c. Figure 5 depicts anomalies in radiative heating due to temperature, moisture and surface temperature anomalies, respectively. Other terms, such as sensible heat flux and horizontal diffusion anomalies, etc., are not large in general (figures not shown), although they could be non-negligible in particular areas to balance other physical mechanisms.

The $(M_{\text{eff}} \nabla \cdot \mathbf{v}_1)'$ has a rather similar pattern to $(M_{q1} \nabla \cdot \mathbf{v}_1)'$, except it is smaller in magnitude (Fig. 4a). It represents the net thermodynamic effect of convergent flow in the atmosphere when the cloud-radiative effect is taken into account [mathematically equivalent to a reduction in effective column-averaged static stability, as seen in (15)]. The actual $(M_1 \nabla \cdot \mathbf{v}_1)'$ is roughly 25% (in magnitude) larger than $(M_{\text{eff}} \nabla \cdot \mathbf{v}_1)'$ in Fig. 4a. The cloud radiative forcing anomalies follow the pattern of precipitation anomalies, with warming (cooling) over the ascending (descending) regions. It is the similarity of this pattern to that of the $(M_1 \nabla \cdot \mathbf{v}_1)'$ that makes the M_{eff} representation useful. The magnitude of the cloud radiative forcing term is up to 24 Wm^{-2} anomalous warming in the eastern Pacific warm area and around 10 Wm^{-2} cooling to the north and 4 Wm^{-2} cooling to the south (Fig. 4b). The anomalous advection of temperature shows a wavy structure in the sub-tropics and mid-latitudes but is small in the tropics (Fig. 4c).

In Fig. 5, the longwave radiative cooling rate includes both effects of outgoing longwave radiation and downward fluxes at surface. The longwave cooling due to temperature anomalies has a similar pattern to tropospheric averaged temperature anomalies (see Fig. 2b). It is on the order of a few Wm^{-2} , with a maximum of 9 Wm^{-2} (Fig. 5a). The troposphere tends to moisten as temperature warms. This causes a small cooling up to 3 Wm^{-2} (Fig. 5b) and the cooling is much more localized than the cooling associated with temperature changes. Outside the ENSO WET area, this term is quite small and changes sign going to mid-latitudes. Over the eastern and central Pacific, positive SST anomalies contribute to tropospheric heating due to increased longwave emission from the surface (Fig. 5c). While only half the magnitude of evaporation anomalies, it is the second largest anomalous warming term in the MSE budget over the ENSO WET region.

Table 2 summarizes the area average of each term in the moist static energy equation for three

target regions. The MSE convergence $(M_1 \nabla \cdot \mathbf{v}_1)'$ is listed first to give an idea of the actual amount. Cloud-radiative forcing as defined in (14) is also shown for completeness. The cloud radiative feedback is then split among other terms as defined in (15). Since the effective MSE convergence provides the most insight into the dynamics, we use the anomalies of $(M_{eff} \nabla \cdot \mathbf{v}_1)'$ as the base value to show the percentage contribution of each physical process in the remainder of Table 2.

For the ENSO WET region, the anomalous MSE divergence is positive because the dry static energy export from the region is somewhat larger than the moisture convergence. The effective MSE divergence anomalies are likewise positive because the cloud radiative warming associated with convergence further reduces it but does not completely overcome the MSE divergence. Overall, this export of energy by the divergent flow tends to balance the heating terms associated with warm SST anomalies, largely latent and sensible heat flux anomalies. Radiative warming excluding cloud effect is small, because the increased surface longwave emission is partly cancelled by enhanced longwave cooling associated with warmer and moister air. Advection of temperature and moisture anomalies are less than 5 Wm^{-2} .

In the NORTH DRY region, there is anomalous convergence of MSE (hence the negative sign) associated with relative descent. Since this is a climatologically convective zone, this corresponds to a reduction in both divergence of dry static energy and moisture convergence. When expressed as an effective moist static energy divergence (including cloud radiative feedbacks), it has a value of -31 Wm^{-2} . Advection of moisture accounts for 15 Wm^{-2} (48%) of the balancing cooling tendency. Anomalous advection of temperature and evaporation are small. The radiative fluxes (not considering clouds) contribute about 7.7 Wm^{-2} cooling.

Over the SOUTH DRY area, the anomalous effective divergence of MSE is -16.7 Wm^{-2} , again a warming tendency associated with descent anomalies (incorporating effects of adiabatic warming, moisture convergence and cloud radiative cooling anomalies). Total advection anomalies (temperature plus moisture) are almost zero in this region. However, reduction of evaporation contributes 9 Wm^{-2} cooling, 53% of the total effective MSE divergence anomalies. For all three regions, the radiative cooling associated with warming of tropospheric temperature is about 20% of the total MSE divergence anomalies.

Overall, the moist static energy budgets in two descent regions demonstrate very different mechanisms for generation of descent anomalies. Over the NORTH DRY region, advection of moisture is the dominant cooling mechanism. However, reduction of surface heat fluxes (mainly, latent heat flux) is the leading effect driving descent anomalies, and thus reduced rainfall, in the SOUTH DRY region. Radiative fluxes provide additional cooling in these anomalously descending areas, but the magnitude of radiative cooling associated with air temperature and moisture changes is smaller than other dominant mechanisms.

Because the moisture advection anomalies involve changes both in horizontal wind and moisture gradient, we further break down the advection anomalies into terms associated with horizontal wind anomalies only, or with moisture gradient only, and residual terms. As shown in the following equation

$$\langle \mathbf{v} \cdot \nabla q \rangle' = \langle \mathbf{v}' \cdot \nabla q^c \rangle + \langle \mathbf{v}^c \cdot (\nabla q)' \rangle + \langle \mathbf{v}' \cdot (\nabla q)' \rangle + \langle \mathbf{v}'' \cdot (\nabla q)'' \rangle \quad (17)$$

where the first term on the r.h.s. $\langle \mathbf{v}' \cdot \nabla q^c \rangle$ denotes the tendency associated with anomalous wind acting on climatological moisture gradient. The second term $\langle \mathbf{v}^c \cdot (\nabla q)' \rangle$ represents the advection due to climatological wind acting on anomalous moisture gradient. The third term $\langle \mathbf{v}' \cdot (\nabla q)' \rangle$ is

the quadratic term associated anomalous wind and moisture gradient, then averaged over the JFM season. $\langle \mathbf{v}'' \cdot (\nabla q)'' \rangle'$ is the residual term due to transient variability.

A similar break-down is applied to evaporation anomalies.

$$\begin{aligned}
E' &= \rho_a C_H V_s' (q_{\text{sat}}(T_s^c) - q_{\text{air}}^c) \\
&+ \rho_a C_H V_s^c (q_{\text{sat}}(T_s) - q_{\text{air}})' \\
&+ \rho_a C_H V_s' (q_{\text{sat}}(T_s) - q_{\text{air}})'' \\
&+ \left(\rho_a C_H \overline{V_s' (q_{\text{sat}}(T_s) - q_{\text{air}})''} \right)' .
\end{aligned} \tag{18}$$

Figure 6 displays the horizontal distribution of two dominant terms in (17). For the NORTH DRY region, it is obvious that $\langle \mathbf{v}' \cdot \nabla q^c \rangle$ is the major contribution to the total moisture advection anomalies (Fig. 6a). This is because the enhanced rising motion near the equator in the eastern Pacific creates a stronger than normal direct thermal circulation in the meridional direction. The northerly return flow anomalies near the surface (see Fig. 2b) bring low moist static energy air into the NORTH DRY region and produce cooling. The term $\langle \mathbf{v}^c \cdot (\nabla q)' \rangle$ has a minimal contribution to the NORTH DRY region per se, although it dries the region further north (Fig. 6b). The quadratic and transient terms are negligible.

For the SOUTH DRY region, the reduction of evaporation is almost evenly contributed by the first two terms in (18). In Fig. 7a, anomalous surface wind acting on climatological air-sea difference creates about 3.6 Wm^{-2} cooling in area average. As shown in Fig. 2b, the prevailing wind anomalies are westerly and southwesterly over the SOUTH DRY region (with climatological easterly wind). This effectively reduces the wind speed in this region. Hence, evaporation is reduced. Furthermore, because of the spreading of moist air into a region with climatological SST, the air-sea moisture difference becomes smaller in the SOUTH DRY region. The climatological wind acting on the reduced air-sea difference produces another 3.6 Wm^{-2} negative evaporation anomalies (Fig. 7b). Other terms are less than 2 Wm^{-2} when averaged over the SOUTH DRY region. In the ENSO WET area, the changes in air-sea difference caused by strong warming of SST dominate the increase of evaporation.

5 Comparison to the NSIPP GCM results

In order to evaluate our model results, we examined the NSIPP GCM model results driven by observed SST from 1930-2000 (Bacmeister et al. 2000; Pegion et al. 2000) for the similar moisture and moist static energy budgets. The outputs from 1982-1998 were used to calculate the climatological means. Anomalies averaged for January-March 1998 were considered, as in previous sections.

Figure 8 illustrates the terms appearing in the moisture equation (2). The precipitation anomalies produced in the NSIPP model (Fig. 8a) resemble the observed Xie-Arkin precipitation anomalies (see Fig. 2b in SNC), although the westward extension of the positive precipitation anomalies is less extensive than in observations. The QTCM has a similar problem. Nevertheless, the reproduction of negative precipitation anomalies to the north and south of the main El Niño warm area is satisfactory. Obviously, the anomalies in the $-\overline{\omega} \partial_p \overline{q}$ term are similar to the precipitation anomalies (Fig. 8b). This is consistent with vertical motion and horizontal divergence anomalies. Because advection of moisture is not a direct model output, we computed $-\nabla \cdot \langle \mathbf{v}' q' \rangle$ and added it to the $-\langle \mathbf{v} \cdot$

$\nabla\bar{q}'$ to include transient variability in the advection anomalies. Overall, moisture advection and evaporation anomalies have patterns very different from that of precipitation anomalies. Considering the area averages over the relative descent region to the north of the El Niño warm area (outlined by -1 mm/day contour of negative precipitation anomalies; likewise for the relative descending region to the south of the warm area), anomalous dry advection of moisture is substantial (Fig. 8c) while the evaporation anomalies have a moistening tendency (Fig. 8d). On the other hand, the area average of moisture advection anomalies to the south of main El Niño warm area is minimal while reduction of evaporation provides significant drying. Within each dry region, anomalies of opposite sign exist but occupy relatively small areas. The area-averaged budgets are highly analogous to the QTCM balances discussed in section 4.2.

The roles of clouds, tropospheric temperature and moisture anomalies in determining the radiative heating rate are hard to assess separately using the available AGCM results. A direct detailed comparison could thus not be made for the MSE budget. Qualitatively, the available MSE analysis suggests different cooling mechanisms forcing descent anomalies over different regions, as in the QTCM.

We also examined the moisture and moist static energy budget for the NCEP/NCAR reanalysis datasets. The anomaly fields of precipitation and moisture convergence during JFM 1998 from the NCEP/NCAR reanalysis bear similar patterns to our model results, although differences exist in details (figures not shown; precipitation anomalies are shown in SNC Fig. 2d). However, the evaporation anomalies from the NCEP/NCAR reanalysis have a rather inconsistent spatial distribution with the overall moisture budget. Trenberth and Guillemot (1998) pointed out that substantial problems exist in the moisture fields of the NCEP/NCAR reanalysis and its moisture budget is not balanced. We likewise find that the moist static energy budget is not even approximately balanced.

One caveat is that both datasets contain response to global SSTs. However, as shown in SNC, the remote response to El Niño positive SST anomalies is the primary signal in the total anomaly fields over the NORTH DRY and SOUTH DRY regions.

6 Composite MSE budget analysis for other El Niño warm events

We have conducted ensemble experiments using positive SST anomalies from three other El Niño events. For compactness, a composite MSE budget is constructed. The three events (1982, 1987 and 1991) were identified in Trenberth (1997). For the ensemble POSPAC runs, we used only three members for each ensemble instead of ten, because of the rather small differences between runs. Due to the variations in the evolution of each warm event, we averaged the period from November to March to accommodate most of the peak warming period. The composite MSE budget terms for the three major El Niño events are shown in Fig. 9.

It is evident that the composite anomaly fields of precipitation, effective MSE divergence, moisture advection and evaporation are strikingly similar to the 1997-1998 case (Fig. 9), except the overall magnitudes are smaller. Instead of using the -1 mm/day contour of negative precipitation anomalies to outline the NORTH DRY and SOUTH DRY regions, we chose -0.5 mm/day contour. Again, in the composite NORTH DRY region, dry anomalies of moisture advection, cancelled partly by positive evaporation anomalies, provide the dominant drying effect in this region. In contrast,

reduced evaporation is the main contribution to the negative precipitation anomalies to the south of the main El Niño warm area, aided to a lesser extent by dry advection. Enhanced evaporation substantially contributes to the anomalous rising motions over the anomalous warm SSTs.

The percentage contribution of each physical process to the total effective MSE divergence anomalies $(M_{\text{eff}} \nabla \cdot \mathbf{v}_1)'$ is shown in Table 3. The results are consistent with the 1997-1998 event with slight differences in exact quantities. The difference in mechanisms for the descent anomalies to the north and south of the main El Niño warm area is substantiated. Similarly, the radiative cooling associated with the warming of the atmosphere accounts for about 20% of the total MSE divergence anomalies. It appears to be a secondary, although non-negligible, forcing for the descent anomalies.

7 Testing impacts of radiative cooling versus other effects

In traditional theory regarding relative descent near regions of warm SST anomalies, increased radiative cooling due to tropospheric warming is key to creating descent anomalies as discussed in the introduction. From our budget study, the nonlocal effects come mainly from the wind field and temperature and moisture fields. Over the NORTH DRY region, it is the advection of moisture that dominates; over the SOUTH DRY region, it is the reduction of evaporation that provides the major “cooling”. The longwave cooling due to tropospheric warming is relatively small, on the order of a few Wm^{-2} , especially over the SOUTH DRY region. Such budgets throw doubt on the traditional view. It is clear that radiative cooling can not directly drive descent anomalies. But perhaps it is still active in initiating descent, with other effects acting as amplifying feedbacks. Can we devise an experiment to eliminate even this hypothesis?

Experiments CLIMRAD.NORTH and CLIMRAD.SOUTH are designed to examine the effect of radiative cooling due to anomalous warming of atmospheric temperature for initiation of descent anomalies. We intervene in the radiative code of the model to disable the radiative cooling associated with temperature anomalies in defined target regions — one for the NORTH DRY region (CLIMRAD.NORTH) and one for the SOUTH DRY region (CLIMRAD.SOUTH). Warm temperature anomalies still occur, but there is no anomalous cooling by infrared effects. Figure 10 shows the results of the two experiments. Compared to Fig. 2a, suppressing the longwave cooling associated with temperature change in the NORTH DRY or SOUTH DRY regions makes little impact on precipitation anomalies. Considering the nonlinearity in the model, it may be possible that the suppression of radiative cooling could be compensated by other terms in the experiments CLIMRAD.NORTH and CLIMRAD.SOUTH. Nevertheless, the radiative cooling associated with temperature change appears to be a secondary forcing in driving descent anomalies and it is not even necessary as an initiator for the occurrence of subsidence anomalies.

For comparison, we conducted sensitivity tests in which the dominant cooling mechanisms in specific regions are suppressed. In the experiment ADV.NORTH, the anomalous advection of temperature and moisture in the NORTH DRY region is suppressed by replacing advection of temperature and moisture by their climatological values (horizontal diffusion is likewise specified to be at its climatological value). In the experiment SFLUX.SOUTH, anomalous sensible and latent heat fluxes in the SOUTH DRY region are suppressed by substituting climatological values of these fluxes. As shown in Fig. 11, suppressing these large “cooling tendencies” in specific

regions has a conspicuous effect: in both regions, negative precipitation anomalies are noticeably smaller than the case without suppressing any anomalous cooling tendencies. In the SOUTH DRY region, the difference is more significant than in the NORTH DRY region. It is interesting to note that in the NORTH DRY region, the negative precipitation anomalies still occur even when advection and diffusion anomalies are suppressed, although with smaller magnitude (Fig. 11a). Terms other than horizontal advection and diffusion, for example evaporation, act to compensate in this experiment and contribute to negative precipitation anomalies to a greater degree than in the POSPAC run. It is possible that determination of descent anomalies may involve dynamical effects such as angular momentum conservation or vorticity balance in addition to thermodynamic constraints. In the SOUTH DRY region, thermodynamic effects are dominant and it is accurate to say that the evaporation anomalies force the descent anomalies.

The finding demonstrated in Fig. 10—that longwave cooling is not the leading factor responsible for the strong descent anomalies—contributes to a developing body of theory in which approximations to temperature response are used. For instance, Neelin and Held (1987), Sobel and Bretherton (2000), and Sobel et al. (2001) use approximations that neglect spatial variations in tropical tropospheric temperature. Zeng and Neelin (1999) uses a local approximation that neglects radiative contributions of temperature anomalies to the MSE budget to determine local precipitation and convergence anomalies in a perturbed region. The current finding shows that temperature anomalies are unimportant to a class of teleconnection phenomenon—strong descent anomalies surrounding heating. We caution, however, that this need not apply to tropical teleconnection in general. SNC notes that some far-field teleconnections affecting winds and surface fluxes appear to be mediated by wave dynamics involving the temperature field.

8 Conclusions

8.1 Summary

Teleconnection mechanisms in relative descent zones are examined using the case of negative precipitation anomalies adjacent to the main El Niño enhanced precipitation region during the 1997-1998 El Niño. Composite budget analysis for three other major El Niño warm events is consistent with the findings for the 1997-1998 case. Simulations were conducted with observed positive SST anomalies only in the tropical Pacific and climatological SST specified in other regions of the model domain. Moisture budget and moist static energy budget analyses over the region of warm SST anomalies and the relative descent zones to the north and south of the El Niño warm area were carried out in the QTCM. The results are qualitatively supported by moisture and moist static energy budgets using the NSIPP atmospheric GCM simulations.

Figure 12 provides a schematic view of the physical processes active in the descent anomaly teleconnection in response to El Niño warm SST forcing. Over the main El Niño warm SST area, increased SST produces greater than normal fluxes of sensible heat, latent heat and upward longwave radiation. In combination with convection, these fluxes maintain a warming through the troposphere in the warm SST region. This warming of the air column is spread by wave dynamics over long distances. The warming produces slightly more longwave flux to space and to the surface but the resulting radiative cooling is small, on the order of a few Wm^{-2} . The anomalous descent

in regions to the north and south of the main El Niño warm area is balanced by different cooling mechanisms. Over the NORTH DRY region, anomalous northerly flow induced by enhanced rising motion and thermally direct circulation brings drier (and colder) air. In the moist static energy budget, the drying tendency by moisture advection anomalies is the dominant process creating a reduction in the divergence of moist static energy and thus forcing descent anomalies. Over the SOUTH DRY region, reduced evaporation due to reduced wind speed and reduced air-sea contrast forces a reduction in the moist static energy divergence, and thus subsidence anomalies. Decreased precipitation in these areas leads to reduced cloud fraction. Cloud-radiation interaction further strengthens the column-averaged cooling due to increased OLR.

The processes in Fig. 12 can also be described using separate moisture and temperature equations although it is more complicated than using the MSE budget. In both regions, the dominant term is a drying tendency: moisture advection anomalies in the NORTH DRY region and evaporation anomalies in the SOUTH DRY region. The drying tendency acts to reduce convective heating, which is balanced by adiabatic warming associated with subsidence anomalies. This reduces moisture convergence which in turn further reduces convective heating and so on, amplifying the original drying tendency. In the MSE budget, the result of this feedback loop is simply taken into account by the gross moist stability, which allows the descent anomalies to be directly obtained given the initial drying tendency. For example, in the NORTH DRY region, the leading contribution to the subsidence anomaly is simply

$$\nabla \cdot \mathbf{v}_1' \approx -(\mathbf{v}' \cdot \nabla q^c) / M_{eff} \quad (19)$$

where the moist static energy budget (15) has been approximated and M_{eff} is the modified gross moist stability that includes cloud radiative feedbacks (16) as well as convective heating feedbacks. The wind anomalies \mathbf{v}' may be approximately taken as given by the heating or convergence in the main ENSO WET region (e.g. Neelin 1988). These wind anomalies spread into the neighboring regions and, where the climatology happens to be conducive, produce drying effects that drive subsidence. The precipitation anomaly can be determined diagnostically from the moisture equation (11) once $\nabla \cdot \mathbf{v}_1'$ is known.

The moist static energy budget results cast doubt on the traditional view of radiative cooling due to tropospheric warming creating descent anomalies in response to a localized heat source. To explicitly test this, experiments were conducted in which anomalous longwave cooling due to increased temperature was suppressed. Little change occurred over the relative descent regions in these experiments, a strong indication that the traditional view is not correct. When the specific cooling mechanisms were suppressed over the NORTH DRY and SOUTH DRY regions, i.e., anomalous advection of temperature and moisture in the NORTH DRY region and anomalous surface heat fluxes in the SOUTH DRY region, negative precipitation anomalies were greatly reduced. This supports our contention that different mechanisms are responsible for the descent anomalies in different regions.

8.2 Theory for compensating descent anomalies

The prevailing assumptions regarding anomalous descending motions are embodied in simplest form in the model of Gill (1980), but is relatively widespread in theory and simple model approaches. Anomalous rising motion associated with convection anomalies leads to warming which tends to be

spread out by tropical wave dynamics reducing pressure gradients. The anomalous warming leads to anomalous infrared cooling which is presumed to cause the anomalous descent with adiabatic warming compensating the cooling.

Comparing data on tropospheric temperature anomalies during an El Niño to the regions of negative precipitation anomalies (Yulaeva and Wallace, 1994; Wallace et al., 1998; SNC), one notes that the spatial patterns do not match well. Furthermore, OLR anomalies associated with changes in cloud fraction are an order of magnitude larger than those associated with temperature anomalies (e.g., Chou and Neelin 1996). Both suggest the processes involved in descent anomalies may be more complex than the traditional view.

Diagnosis of the runs discussed above suggests a substantial revision to the theory of descent anomalies. An example is schematized in Fig. 13 for the case of teleconnected response to positive El Niño SST in the Pacific. The schematic is based on experiments with no anomalies in other basins and no negative anomalies in the Pacific [which otherwise would contribute additional western Pacific negative precipitation anomalies (see SNC)]. The tropospheric warming associated with positive El Niño SST anomalies extends over a large region. However, the regions of reduced precipitation (and anomalous descent) occur in relatively localized regions within the anomalous warm region. Both of these aspects correspond to observations.

The hypothesized dynamics for this is as follows. The heat fluxes associated with warm SST anomalies are carried through a deep layer by convection, setting an anomalously warm tropospheric temperature over that region. Rossby and Kelvin wave dynamics act to smooth out the baroclinic pressure gradient that would otherwise occur. Since much of the region of response is within convective zones, the wave dynamics is strongly modified by convective and cloud-radiative feedbacks and is best regarded as moist wave dynamics in those regions. The overall effect, however, is to extend the tropospheric warming over a large region. In the traditional mechanism, anomalous descent would occur over this region with radiative cooling balancing the adiabatic warming of anomalous descent. However, the radiative anomalies associated with the tropospheric warming are quite small, on the order of a few Wm^{-2} , and produce only tiny descent anomalies. Instead, the descent tends to occur in particular regions where larger “cooling tendencies” act. We place cooling tendencies in quotations because in convection zones, these cooling terms can include moisture advection, $\mathbf{v} \cdot \nabla q$, or evaporation anomalies, which enter via changes in convective heating since the deep convection links the moisture budget and the temperature budget. The descent anomalies over the eastern equatorial South America appear to be a remote response to the El Niño warm SST anomalies (see Fig. 2a). Its mechanism is analyzed separately because it involves land-surface processes, which add additional feedbacks in the teleconnection system.

In this explanation, the tropospheric warming associated with positive El Niño SST anomalies can extend over a large region precisely because the associated radiative cooling is weak. The associated wave dynamics can thus potentially communicate some teleconnection effects over very large distances. The strongest teleconnections to descent anomalies occur within shorter distances and fundamentally involve moist thermodynamics. These mechanisms create a dependence on the climatology of winds, rainfall and moisture, and on the teleconnected wind and moisture anomalies surrounding the SST forcing region. Thus the pattern of the descending motion surrounding a warm SST anomaly can be expected to be sensitive to the location and details of the forcing. This potentially makes the simulation and forecast of descent anomalies even more challenging than that of direct enhanced precipitation anomalies in warm SST areas.

Acknowledgments. This work was supported under National Science Foundation Grant ATM-0082529, National Oceanographic and Atmospheric Administration Grant NA16-GP2003 and National Aeronautics and Space Administration Grant NA-GS-9358. This is UCLA IGPP contribution 5685. The authors thank M. Suarez, M. Rienecker, P. Pegion, M. Kistler and the NASA Seasonal-to-Interannual Prediction Project (NSIPP) for access to NSIPP AGCM simulation results, J. E. Meyerson for graphical assistance, C. Chou for improvements to the radiative code, M. Munnich for discussions and K. Hales for improvements of the manuscript.

REFERENCES

- Bacmeister, J., P. J. Pegion, S. D. Schubert, and M. J. Suarez, 2000: *Atlas of Seasonal Means Simulated by the NSIPP 1 Atmospheric GCM*, TM-2000-104606, Vol.17, NASA, 192 pp.
- Barnett, T. P., L. Bengtsson, K. Arpe, M. Flügel, N. Graham, M. Latif, J. Ritchie, E. Roeckner, U. Schlese, U. Schulzweida and M. Tyrée, 1994: Forecasting global ENSO-related climate anomalies. *Tellus*, **46A**, 381–397.
- Barnston, A.G., A. Leetmaa, V.E. Kousky, R.E. Livezey, E.A. O’Lenic, H.V. den Dool, A.J. Wagner, and D.A. Unger, 1999: NCEP Forecasts of the El Niño of 1997-98 and its U.S. impacts. *Bull. Amer. Meteor. Soc.*, **80**, 1829–1852.
- Charney, Jule G., 1959: On the general circulation of the atmosphere. *The Atmosphere and the Sea in Motion*, Rockefeller Institute Press, New York, N.Y., pp. 178-193.
- Chou, C., and J. D. Neelin, 1996: Linearization of a long-wave radiation scheme for intermediate tropical atmospheric models. *J. Geophys. Res.*, **101**, 15129-15145.
- Chou, C., 1997: Simplified radiation and convection treatments for large-scale tropical atmospheric modeling. Ph.D. Dissertation, University of California, Los Angeles, 215pp.
- Farrara, J. D., C. R. Mechoso, and A. W. Robertson, 2000: Ensembles of AGCM two-tier predictions and simulations of the circulation anomalies during winter 1997-98. *Mon. Wea. Rev.*, **128** 3589–3604.
- Frederiksen, C. S., H. Zhang, R. C. Balgovind, N. Nicholls, W. Drosowsky, and L. Chambers, 2001: Dynamical seasonal forecasts during the 1997/98 ENSO using persisted SST anomalies. *J. Climate*, *Accepted*.
- Gill, A. E., 1980: Some simple solutions for heat induced tropical circulation. *Quart. J. Roy. Meteor. Soc.*, **106**, 447–462.
- Goddard, L. and N. E. Graham, 1999: The importance of the Indian ocean for simulating rainfall anomalies over eastern and southern Africa. *J. Geophys. Res.*, **104**, 19099–19116.
- Held, I. M., S. W. Lyons, and S. Nigam, 1989: Transients and the extratropical response to El Niño. *J. Atmos. Sci.*, **46**, 163–176.
- Hoerling, M. P., and M.-F. Ting, 1994: Organization of extratropical transients during El Niño. *J. Climate*, **7**, 745–766.
- Hoskins, B.J.; and D. J. Karoly, 1981: The steady linear response of a spherical atmosphere to thermal and orographic forcing. *J. Atmos. Sci.*, **38**, 1179–1196.
- Kalnay, E., et al., 1996: The NCEP/NCAR 40-year reanalysis project. *Bull. Amer. Meteor. Soc.*, **77**, 437–471.
- Kumar, A. and M. P. Hoerling, 1998: Specification of regional sea surface temperatures in the atmospheric general circulation model simulations. *J. Geophys. Res.*, **103**, 8901–8907.
- Latif, M, D. Dommenges, M. Dima, and A. Grotzner, 1999: The role of Indian ocean sea surface temperature in forcing east African rainfall anomalies during December-January 1997/98. *J. Climate*, **12**, 3497–3504.
- Lau, N.-C., 1985: Modeling the seasonal dependence of the atmospheric response to observed El Niños in 1962-76. *Mon. Wea. Rev.*, **113**, 1970–1996.
- Matsuno, T., 1966, Quasi-geostrophic motions in the equatorial areas. *J. Meteor. Soc. Japan*, **44**, 25–43.

- Mechoso, C. R., A. Kitoh, S. Moorthi and A. Arakawa, 1987: Numerical simulations of the atmospheric response to a sea surface temperature anomaly over the equatorial eastern Pacific Ocean. *Mon. Wea. Rev.*, **115**, 2936–2956.
- Neelin, J. D., 1997: Implications of convective quasi-equilibrium for the large-scale flow. In *The physics and parameterization of moist atmospheric convection*. R. K. Smith, ed., Kluwer Academic Publishers, Dordrecht, The Netherlands, pp. 413-446.
- Neelin, J. D., and I. M. Held, 1987: Modeling tropical convergence based on the moist static energy budget. *Mon. Wea. Rev.*, **115**, 3–12.
- Neelin, J. D., 1988: A simple model for surface stress and low-level flow in the tropical atmosphere driven by prescribed heating. *Quart. J. Roy. Meteor. Soc.*, **114**, 747–770.
- Neelin, J. D. and N. Zeng, 2000: A quasi-equilibrium tropical circulation model—Formulation. *J. Atmos. Sci.*, **57**, 1741–1766.
- Pegion, P. J., S.D. Schubert, and M.J. Suarez, 2000: *An Assessment of the Predictability of Northern Winter Seasonal Means with the NSIPP 1 AGCM*. TM-2000-104606, Vol. 18, NASA.
- Rodwell, M. J., and Hoskins, B. J., 1996: Monsoons and the dynamics of deserts. *Quart. J. Roy. Meteor. Soc.*, **122**, 1385–1404.
- Ropelewski, C. F. and M. S. Halpert, 1987: Global and regional scale precipitation associated with El Niño/Southern Oscillation. *Mon. Wea. Rev.*, **115**, 1606–1626.
- Salby, M. L. and R. R. Garcia, 1987: Transient response to localized episodic heating in the tropics. I. Excitation and short-time near-field behavior. *J. Atmos. Sci.*, **44**, 458–498.
- Saravanan, R. and P. Chang, 2000: Interaction between tropical Atlantic variability and El Niño–Southern Oscillation. *J. Climate*, **13**, 2177– 2194.
- Simmons, A. J., J. M. Wallace, G. W. Branstator, 1983: Barotropic wave propagation and instability, and atmospheric teleconnection patterns. *J. Atmos. Sci.*, **40**, 1363–1392.
- Sobel, A. H., and C. S. Bretherton, 2000: Modeling tropical precipitation in a single column. *J. Climate*, **13**, 4378–4392.
- Sobel, A. H., J. Nilsson, and L. M. Polvani, 2001: The weak temperature gradient approximation and balanced tropical moisture waves. *J. Atmos. Sci.*, **58**, 3650-3665.
- Soden, B. J., 2000: The sensitivity of the tropical hydrological cycle to ENSO. *J. Climate*, **13**, 538–549.
- Straus, D. M. and J. Shukla, 1997: Variations of midlatitude transient dynamics associated with ENSO. *J. Atmos. Sci.*, **54**, 770–790.
- Su, H., J. D. Neelin, and C. Chou, 2001: Tropical teleconnection and local response to SST anomalies during the 1997-1998 El Niño. *J. Geophys. Res.*, **106**, 20,025-20,043.
- Trenberth, K. E., 1997: The definition of El Niño. *Bull. Amer. Meteor. Soc.*, **78** 2771–2777.
- Trenberth, K. E., G. W. Branstator, D. Karoly, A. Kumar, N.-C. Lau and C. Ropelewski, 1998: Progress during TOGA in understanding and modeling global teleconnections associated with tropical sea surface temperatures. *J. Geophys. Res.*, **103**, 14291–14324.
- Trenberth, K. E., and C. J. Guillemot, 1998: Evaluation of the atmospheric moisture and hydrological cycle in the NCEP/NCAR reanalysis, *Climate Dynamics*, **14**, 213-231.
- Wallace, J. M. and D. S. Gutzler, 1981: Teleconnections in the potential height field during the Northern Hemisphere winter. *Mon. Wea. Rev.*, **109**, 784–812.
- Wallace, J. M., E. M. Rasmusson, T. P. Mitchell, V. E. Kousky, E. S. Sarachik and H. von Storch, 1998: On the structure and evolution of ENSO-related climate variability in the tropical

Pacific: Lessons from TOGA, *J. Geophys. Res.*, **103**, 14241–14260.

Webster, P. J., 1972: Response of the tropical atmosphere to local steady forcing. *Mon. Wea. Rev.*, **100**, 518–540.

Webster, P. J. and H.-R. Chang, 1988: Equatorial energy accumulation and emanation regions: Impacts of a zonally varying basic state. *J. Atmos. Sci.*, **45**, 803–829.

Yu, J.-Y., C. Chou and J. D. Neelin, 1998: Estimating the gross moist stability of the tropical atmosphere. *J. Atmos. Sci.*, **54**, 1054–1063.

Yulaeva, E. and J. M. Wallace, 1994: The signature of ENSO in global temperature and precipitation fields derived from the microwave sounding unit, *J. Climate*, **7**, 1719–1736.

Xie, P, and P.A. Arkin, 1997: Global precipitation: A 17-year monthly analysis based on gauge observations, satellite estimates and numerical model outputs. *Bull. Amer. Meteor. Soc.*, **78**, 2539–2558.

Zeng, N., and J. D. Neelin, 1999: A land-atmosphere interaction theory for the tropical deformation problem. *J. Climate*, **12**, 857–872.

Zeng, N., J. D. Neelin and C. Chou, 2000: A quasi-equilibrium tropical circulation model—implementation and simulation. *J. Atmos. Sci.*, **57**, 1767–1796.

FIGURE CAPTIONS

Figure 1: Anomalies of 500 hPa vertical pressure velocity ω during JFM 1998 from (a) NCEP/NCAR reanalysis, contour interval 20×10^{-3} Pa/s with dark shading below -20 and light shading above 20; (b) the QTCM simulation with observed global ($60^{\circ}\text{S} - 60^{\circ}\text{N}$) SST anomalies, contour interval 8×10^{-3} Pa/s with dark shading below -8 and light shading above 8; and (c) the POSPAC run, contour interval and shadings as Fig. 1b.

Figure 2: Model-simulated anomalies in the POSPAC run during JFM 1998: (a) precipitation, contour interval 1 mm day^{-1} with dark shading above 1 and light shading below -1; (b) tropospheric temperature and 850 hPa winds, contour interval 0.25 C with light shading above 0.25 and dark shading above 0.75, and wind vectors in m s^{-1} ; and (c) OLR, contour interval 5 Wm^{-2} with dark shading below -5 and light shading above 5.

Figure 3: The horizontal distribution of (a) $(M_{q1} \nabla \cdot \mathbf{v}_1)'$, contour interval 20 Wm^{-2} with dark shading above 20 and light shading below -20; (b) $-\langle \mathbf{v} \cdot \nabla q \rangle'$, contour interval 5 Wm^{-2} with dark shading above 5 and light shading below -5; and (c) E' , contour interval and shadings as Fig. 3b. The dark outlined regions are the ENSO WET (I), NORTH DRY (II) and SOUTH DRY (III) regions, respectively.

Figure 4: The horizontal distribution of (a) $(M_{eff} \nabla \cdot \mathbf{v}_1)'$, contour interval 5 Wm^{-2} with dark shading above 5 and light shading below -5; (b) atmospheric radiative heating rate due to clouds, CRF' , contour interval 2 Wm^{-2} with dark shading above 2 and light shading below -2; and (c) $-\langle \mathbf{v} \cdot \nabla T \rangle'$, contour interval and shadings as Fig. 4a.

Figure 5: The atmospheric longwave radiative heating rate due to (a) temperature anomalies, $\epsilon_T T_1'$, contour interval 1 Wm^{-2} with light shading below -1 and dark shading above 1; (b) moisture anomalies, $\epsilon_q q_1'$, contour interval and shadings as Fig. 5a; and (c) surface temperature changes, $\epsilon_{T_s} T_s'$, contour interval 5 Wm^{-2} and shaded above 5.

Figure 6: The break-down of moisture advection anomalies: (a) $-\mathbf{v}' \cdot \nabla q^c$ (the tendency associated with anomalous wind acting on climatological moisture gradient), contour interval 5 Wm^{-2} with light shading below -5 and dark shading above 5; and (b) $-\mathbf{v}^c \cdot (\nabla q)'$ (the advection due to climatological wind acting on anomalous moisture gradient), contour interval and shadings as Fig. 6a. The NORTH DRY region is shown in dark outline.

Figure 7: The break-down of evaporation anomalies: (a) $\rho_a C_H V_s' (q_{\text{sat}}(T_s^c) - q_{\text{air}}^c)$ (the evaporation anomalies due to changes of surface wind speed acting with climatological air-sea moisture difference), contour interval 2 Wm^{-2} with light shading below -2 and dark shading above 2; and (b) $\rho_a C_H V_s^c (q_{\text{sat}}(T_s) - q_{\text{air}})'$ (the evaporation anomalies due to changes in air-sea moisture difference acting with climatological wind speed), contour interval 2 Wm^{-2} for negative anomalies with light shading below -2 and 10 Wm^{-2} for positive anomalies with dark shading above 2. The SOUTH DRY region is shown in dark outline.

Figure 8: The horizontal distribution of the anomaly fields from the NSIPP AGCM simulations: (a) precipitation, contour interval 1 mm day^{-1} with dark shading above 1 and light shading below -1; (b) vertical advection of moisture (moisture convergence), contour interval 50 Wm^{-2} with dark shading above 50 and light shading below -50; (c) horizontal advection of moisture, contour interval 20 Wm^{-2} with light shading below -20 and dark shading above 20; and (d) evaporation, contour interval 10 Wm^{-2} with dark shading above 10 and light shading below -10.

Figure 9: The composite MSE budget for the three El Niño warm events (1982, 1987 and 1991)

averaged for November-March: (a) precipitation anomalies, contour interval 0.5 mm day^{-1} with dark shading above 0.5 and light shading below -0.5 ; (b) $(M_{eff} \nabla \cdot \mathbf{v}_1)'$, contour interval 5 Wm^{-2} with dark shading above 5 and light shading below -5 ; (c) $-(1 + C)\langle \mathbf{v} \cdot \nabla q \rangle'$, contour interval 4 Wm^{-2} with dark shading above 4 and light shading below -4 ; and (d) $(1 + C)E'$, contour and shading same as (c).

Figure 10: As in Fig. 2a but for precipitation anomalies simulated in the CLIMRAD.NORTH and CLIMRAD.SOUTH runs. The NORTH DRY and SOUTH DRY regions are shown in dark outline in Fig. 9a and 9b, respectively.

Figure 11: As in Fig. 2a but for precipitation anomalies simulated in the ADV.NORTH and SFLUX.SOUTH runs. The NORTH DRY and SOUTH DRY regions are shown in dark outline in Fig. 10a and 10b, respectively.

Figure 12: Mechanisms for El Niño-related teleconnections to descent anomaly regions in the tropical Pacific. Vertical arrows indicate the direction of fluxes. The thick arrows represent the dominant mechanisms for the descent anomalies over the target regions (and surface flux forcing in the anomalous ascent region). The thinner arrows show longwave cloud-radiative effects. The dashed arrows indicate the radiative cooling associated with the warming of atmosphere.

Figure 13: Schematic diagram of a revised view of the teleconnections in the neighborhood of El Niño warm SST anomalies, emphasizing the separation between tropospheric warming and the mechanisms driving descent anomalies. The relative importance of the descent mechanisms indicated can vary among regions (see Fig. 12) and teleconnection events.

Table 1: Area-averaged moisture budget anomalies for three target regions for the POSPAC run. Values are in W m^{-2} . Numbers in parenthesis give percentage values relative to the area-averaged precipitation anomalies, $Prec'$.

	ENSO WET	NORTH DRY	SOUTH DRY
$Prec'$	101.6 (100%)	-70.2 (100%)	-41.0 (100%)
$(M_{q1} \nabla \bullet \mathbf{v}_1)'$	80.6 (79%)	-52.8 (75%)	-30.3 (73%)
$-\langle \mathbf{v} \bullet \nabla q \rangle'$	2.0 (2%)	-13.3 (19%)	-1.3 (3%)
E'	21.6 (21%)	0.5 (-0.7%)	-7.9 (19%)

Table 2: Area-averaged moist static energy budget anomalies for three target regions for the POSPAC run. Values are in W m^{-2} . Numbers in parenthesis give percentage values relative to the area-averaged effective MSE divergence anomalies, $(M_{eff} \nabla \bullet \mathbf{v}_1)'$.

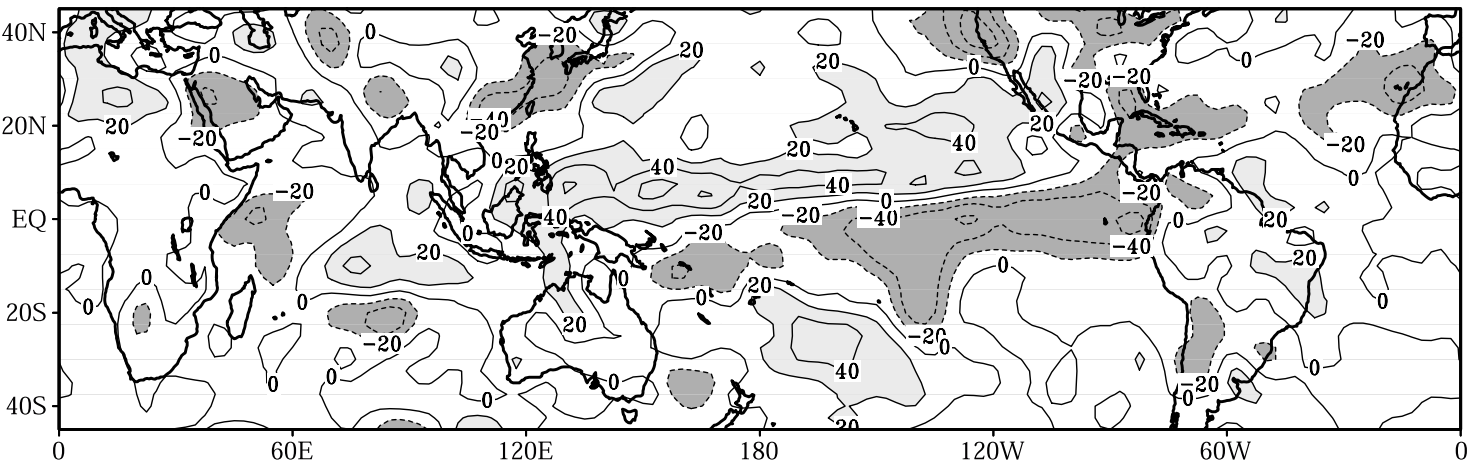
	ENSO WET	NORTH DRY	SOUTH DRY
$(M_1 \nabla \bullet \mathbf{v}_1)'$	48.0	-37.5	-20.4
CRF'	12.2	-8.0	-5.0
$(M_{eff} \nabla \bullet \mathbf{v}_1)'$	38.2 (100%)	-31.1 (100%)	-16.7 (100%)
$-\langle \mathbf{v} \bullet \nabla T \rangle'$	2.5 (7%)	-1.4 (5%)	1.5 (-9%)
$-(1 + C) \langle \mathbf{v} \bullet \nabla q \rangle'$	2.2 (6%)	-15.0 (48%)	-1.5 (9%)
$(1 + C)E'$	24.2 (63%)	0.6 (-2%)	-8.9 (53%)
H'	9.5 (25%)	-4.7 (15%)	-2.1 (13%)
$\varepsilon_{T1} T_1'$	-6.2 (-16%)	-6.9 (22%)	-3.2 (19%)
$\varepsilon_{q1} q_1'$	-2.3 (-6%)	-0.8 (3%)	-0.7 (4%)
$\varepsilon_{Ts} T_s'$	12.9 (34%)	0.0 (0%)	0.0 (0%)

Table 3: Area-averaged moist static energy budget anomalies for three target regions based on the composite POSPAC runs of three major El Niño events (1982, 1987 and 1991). Values are in W m^{-2} . Numbers in parenthesis give percentage values relative to the area-averaged effective MSE divergence anomalies, $(M_{eff} \nabla \bullet \mathbf{v}_1)'$. The boundaries of the NORTH DRY and SOUTH DRY regions are determined by the -0.5 mm day^{-1} contour of precipitation anomalies.

	ENSO WET	NORTH DRY	SOUTH DRY
$(M_{eff} \nabla \bullet \mathbf{v}_1)'$	24.7 (100%)	-10.6 (100%)	-9.6 (100%)
$-\langle \mathbf{v} \bullet \nabla T \rangle'$	1.0 (4%)	-0.9 (8%)	0.6 (-6%)
$-(1 + C) \langle \mathbf{v} \bullet \nabla q \rangle'$	2.0 (8%)	-4.8 (45%)	-1.3 (13%)
$(1 + C)E'$	16.1 (65%)	0.2 (-2%)	-4.0 (41%)
H'	6.6 (27%)	-1.2 (11%)	-1.3 (13%)
$\varepsilon_{T1} T_1'$	-4.5 (-18%)	-3.0 (28%)	-2.5 (26%)
$\varepsilon_{q1} q_1'$	-1.7 (-7%)	-0.5 (4%)	-0.5 (5%)
$\varepsilon_{Ts} T_s'$	9.0 (36%)	0.8 (8%)	0.3 (3%)

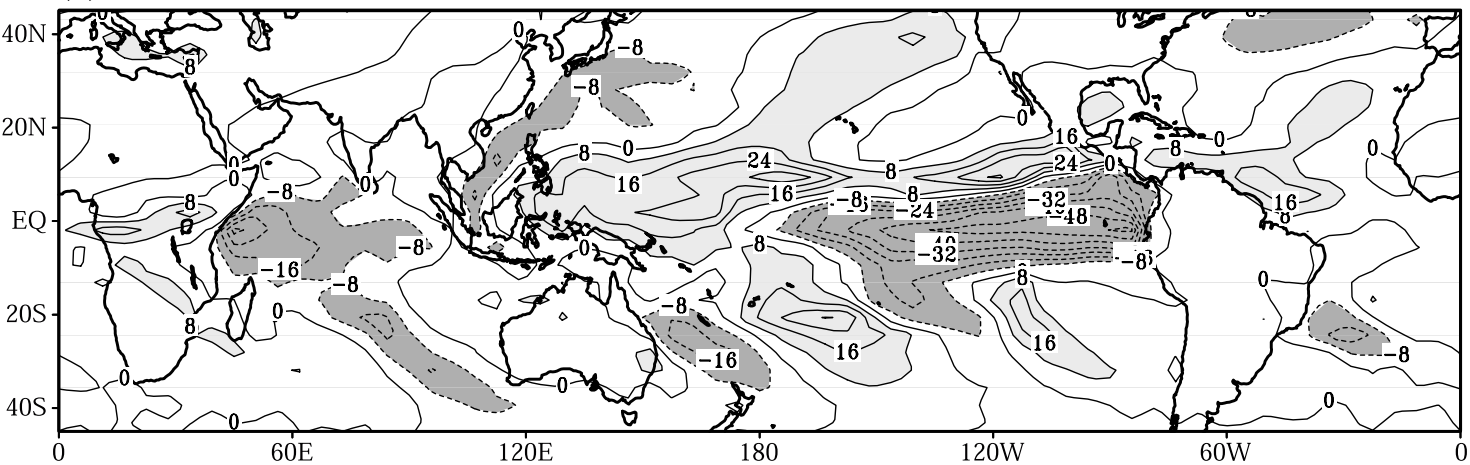
(a) 500 hPa ω Anomalies JFM 1998

NCEP/NCAR



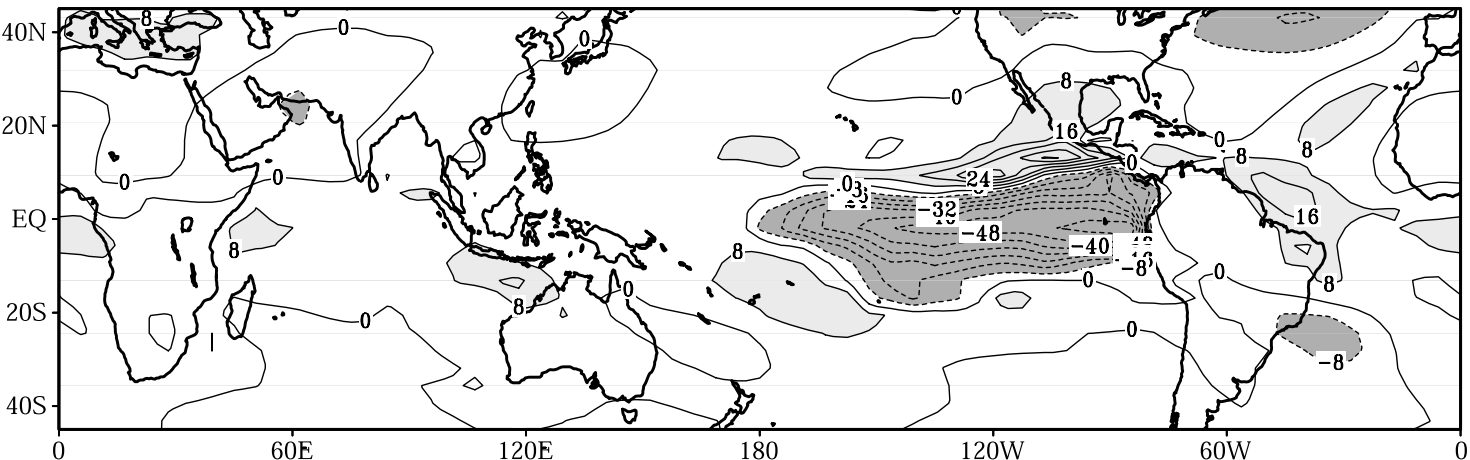
(b) 500 hPa ω Anomalies JFM 1998

OBSSST - CLIM

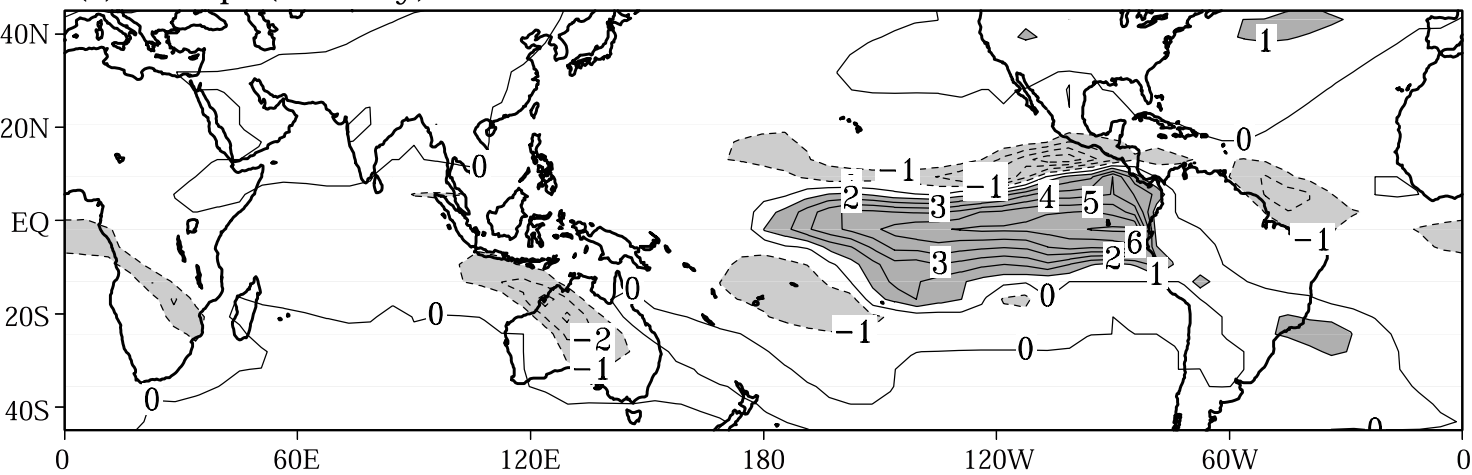


(c) 500 hPa ω Anomalies JFM 1998

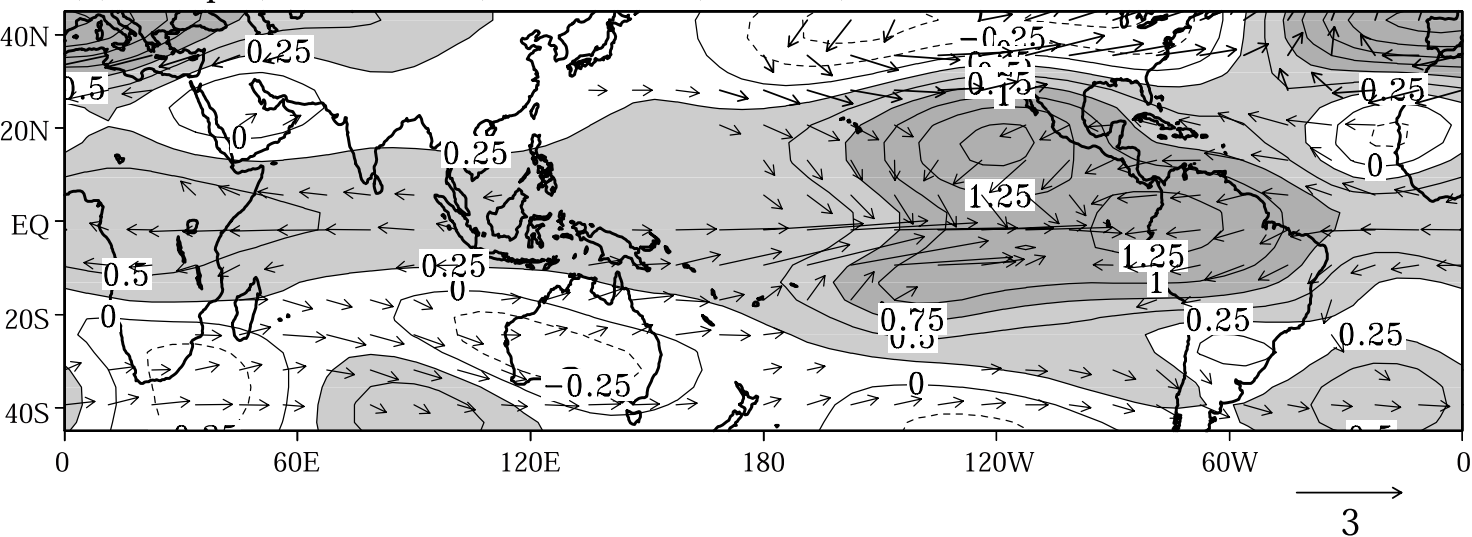
POSPAC - CLIM



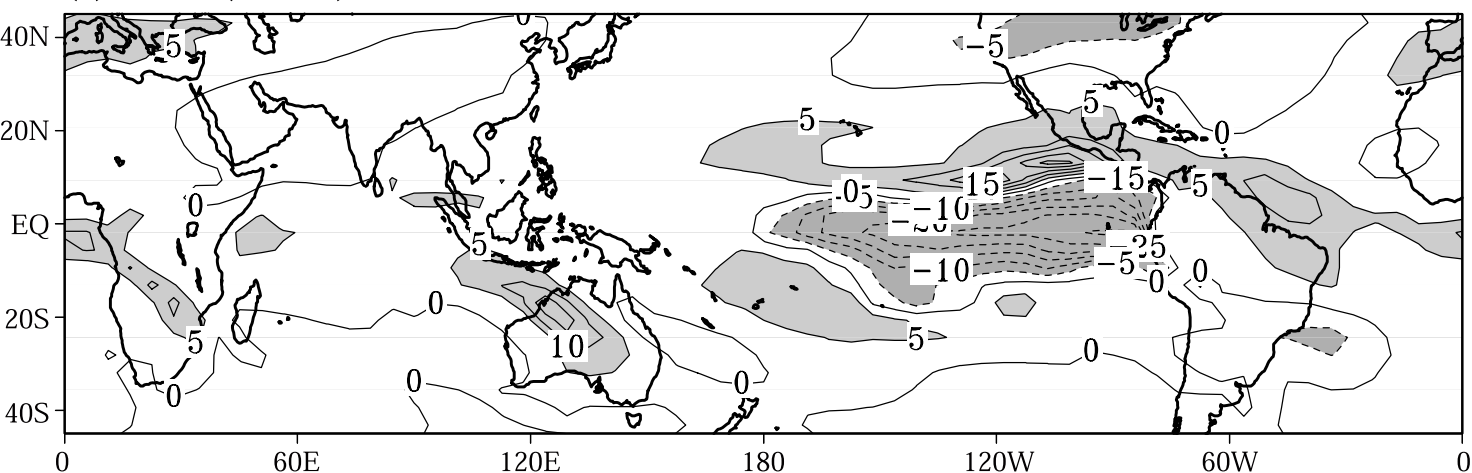
(a) Precip. (mm/day) JFM 1998 POSPAC - CLIM



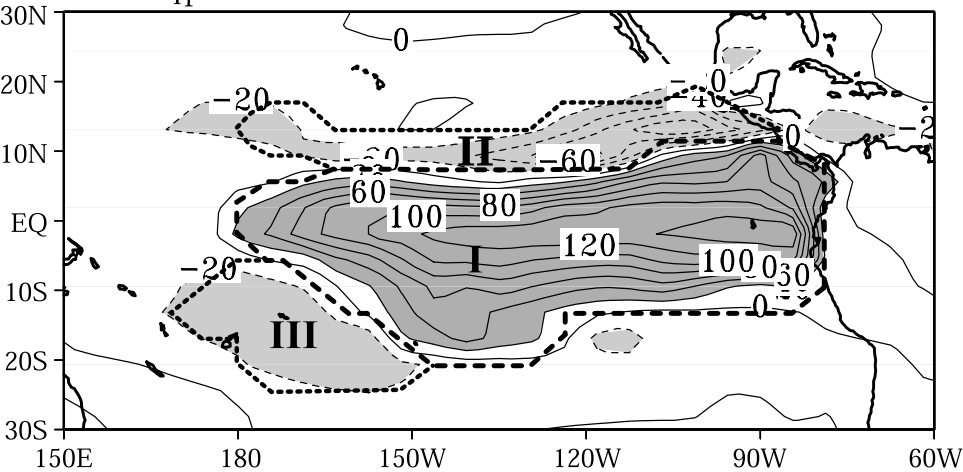
(b) Temp. (850-200 hPa) and Wind (850 hPa)



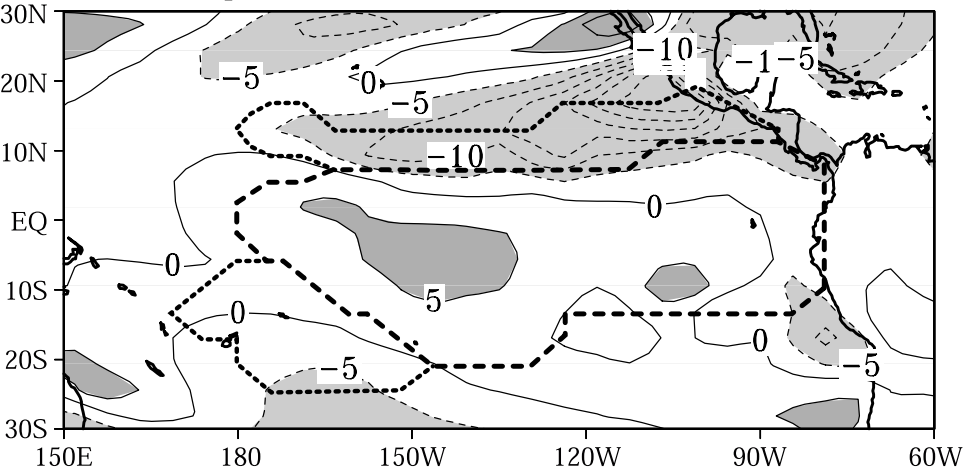
(c) OLR (W/m^2)



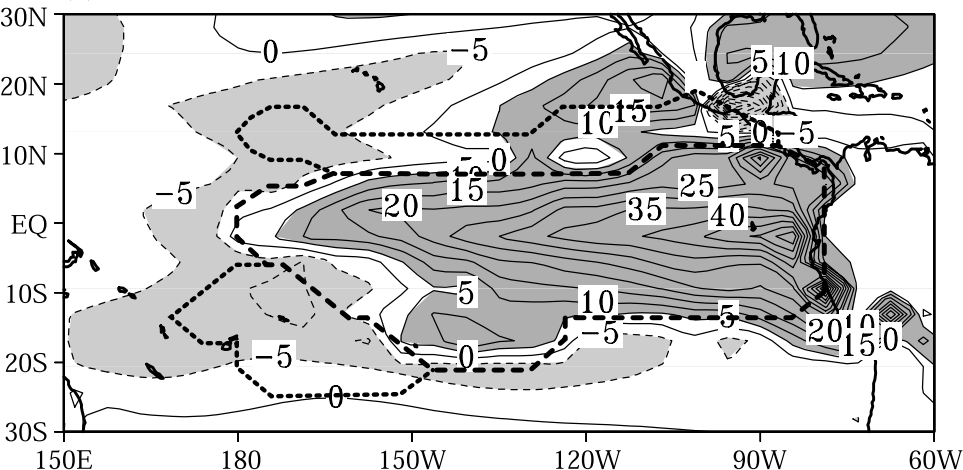
(a) $(M_{q_1} \nabla \cdot \mathbf{v}_1)'$ (W/m^2) JFM 1998 POSPAC - CLIM



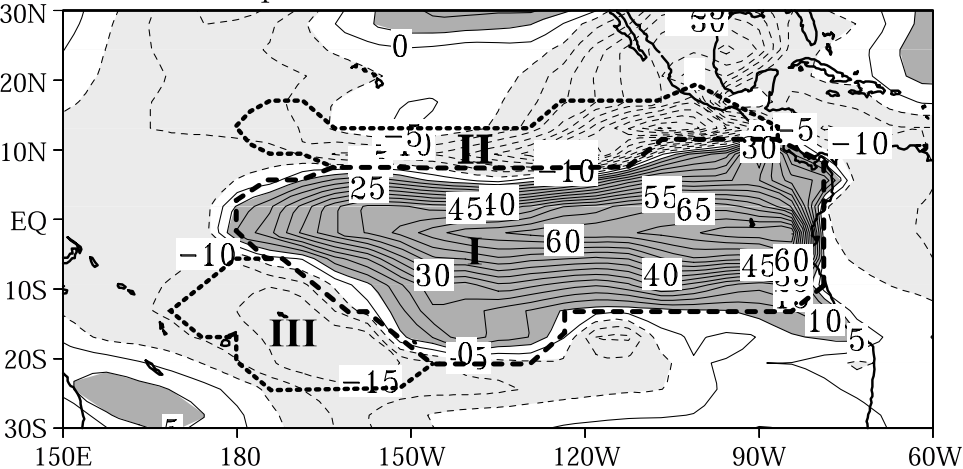
(b) $-\langle \mathbf{v} \cdot \nabla q \rangle'$



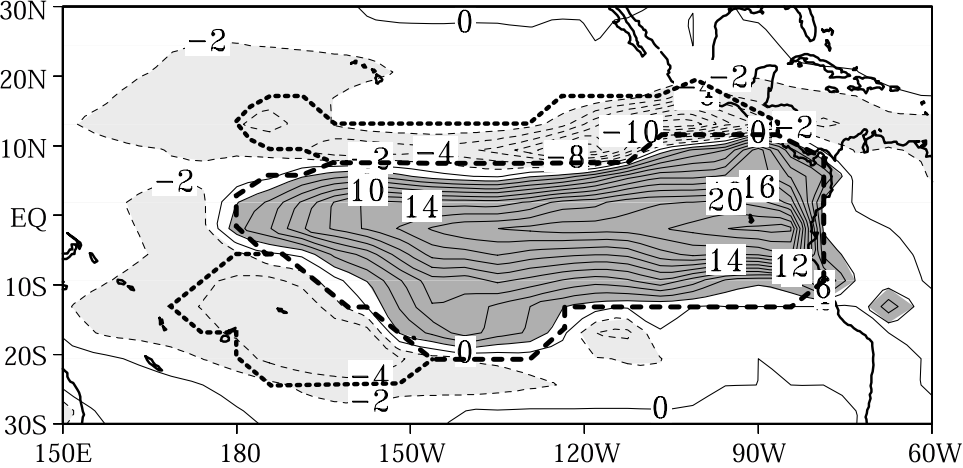
(c) E'



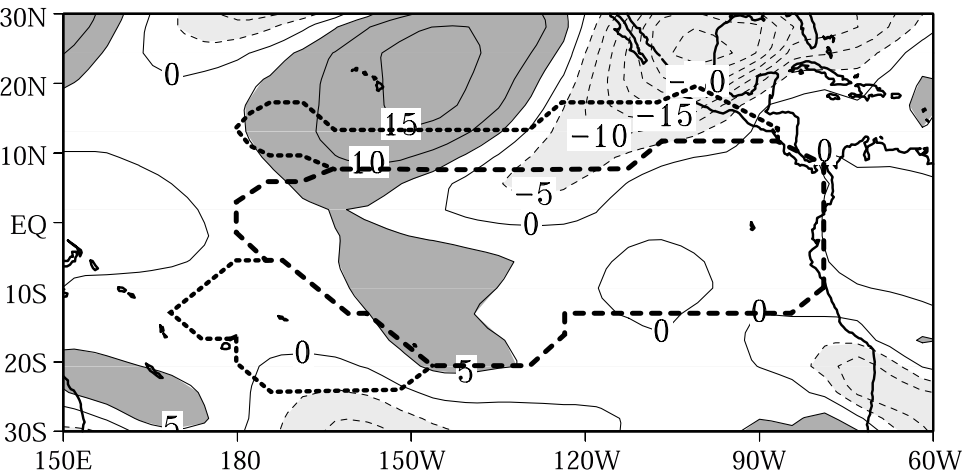
(a) $(M_{\text{eff}} \nabla \cdot \mathbf{v}_1)'$ (W/m^2) JFM 1998 POSPAC - CLIM



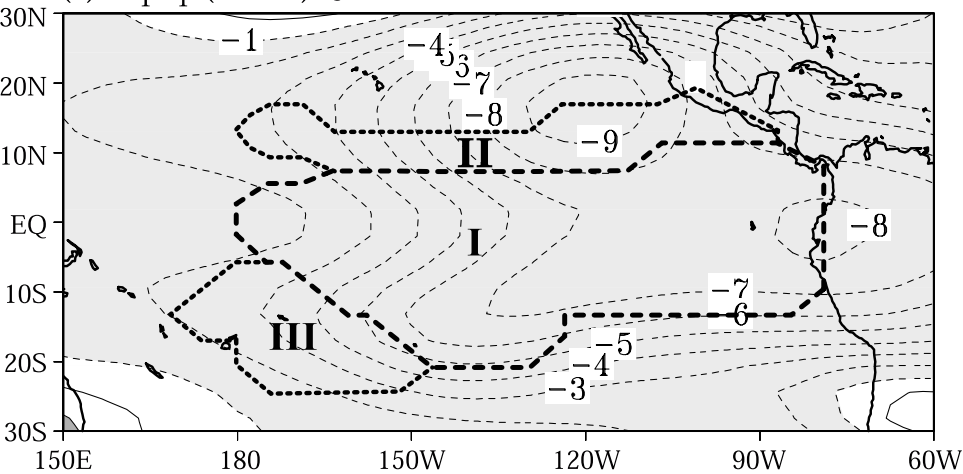
(b) CRF'



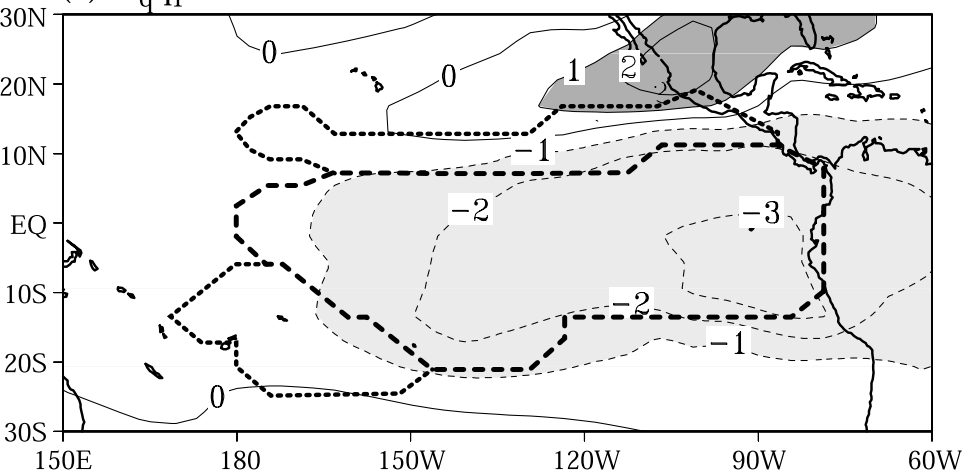
(c) $-\langle \mathbf{v} \cdot \nabla T \rangle'$



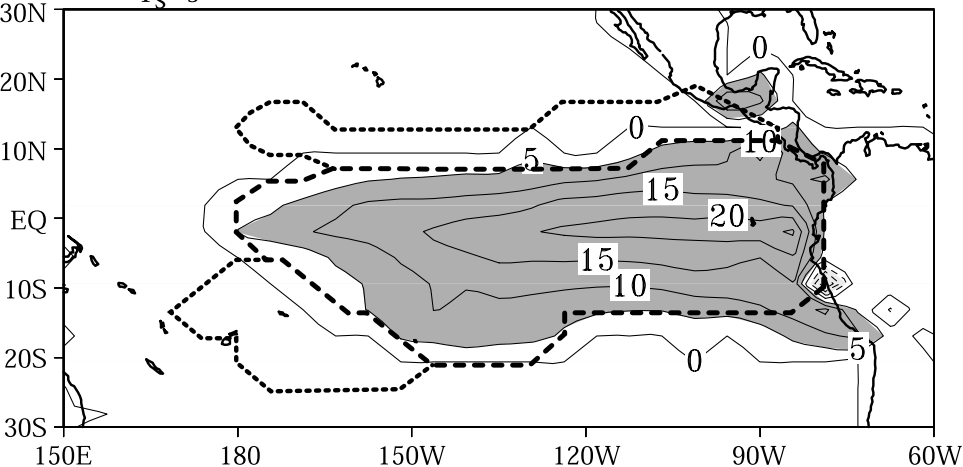
(a) $\varepsilon_T T_1'$ (W/m^2) JFM 1998 POSPAC - CLIM



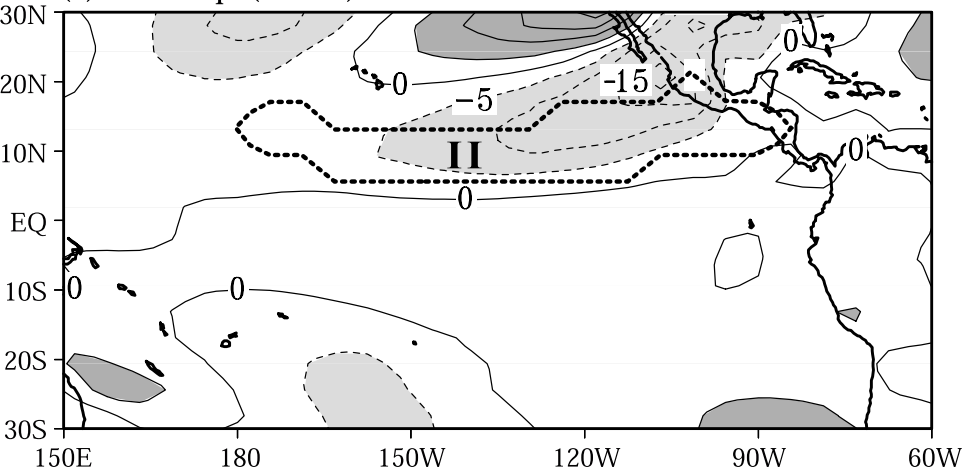
(b) $\varepsilon_q q_1'$



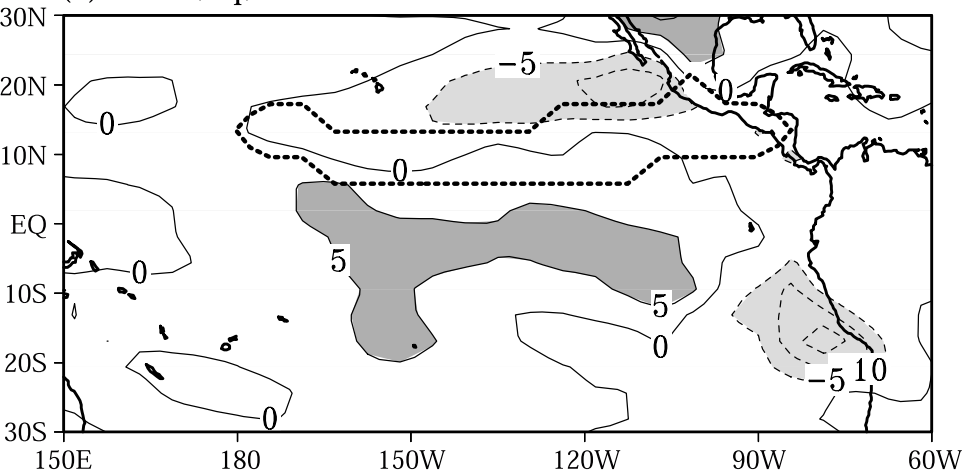
(c) $\varepsilon_{T_s} T_s'$

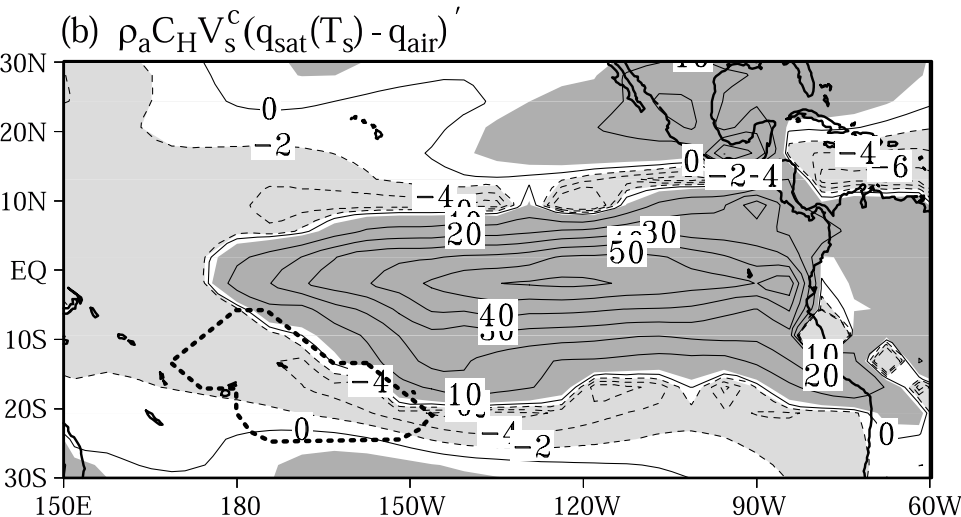
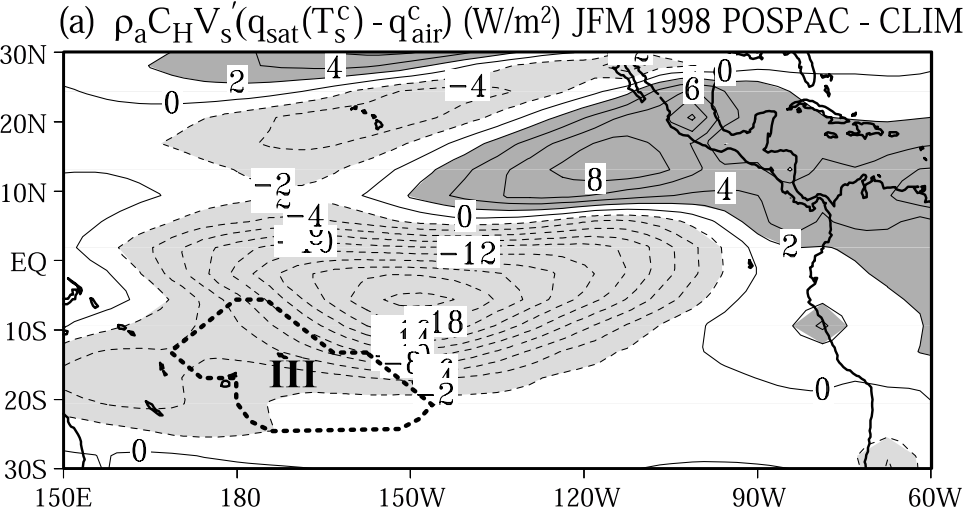


(a) $-\mathbf{v}' \cdot \nabla q^c$ (W/m^2) JFM 1998 POSPAC - CLIM

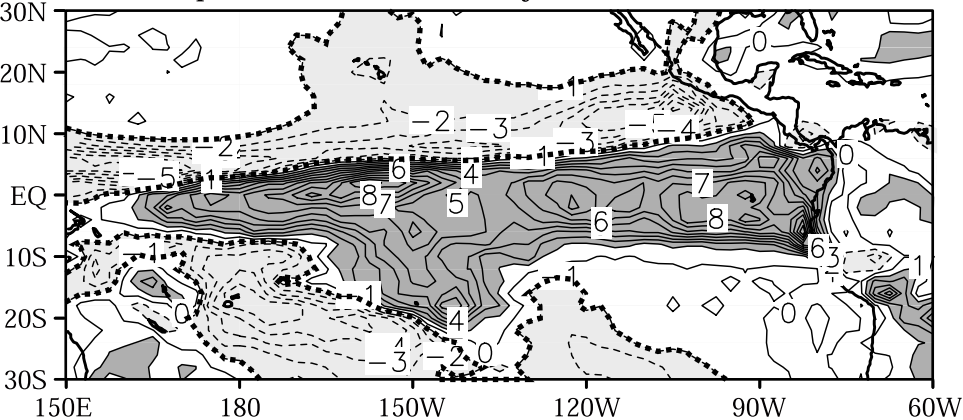


(b) $-\mathbf{v}^c \cdot (\nabla q)'$

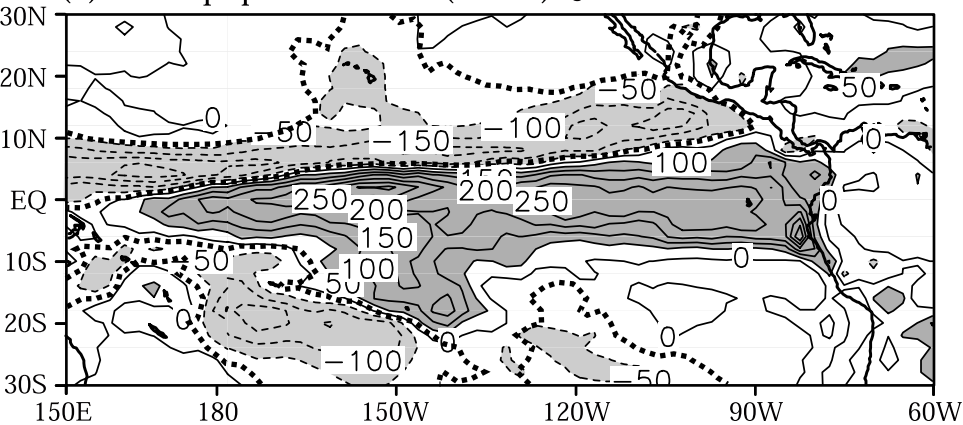




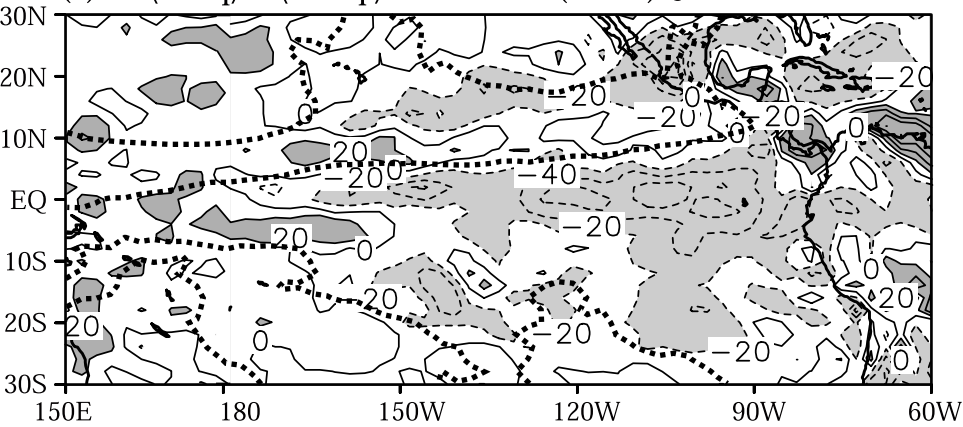
(a) Precip. Anomalies (mm/day) JFM 1998 NSIPP



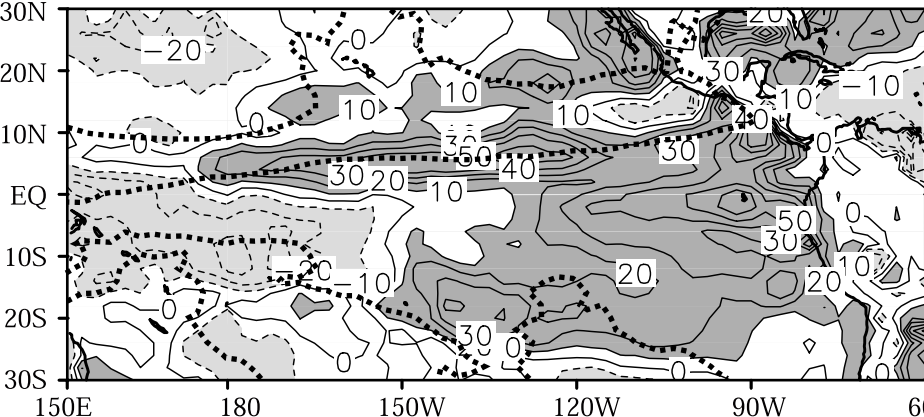
(b) $-\overline{\omega\partial\bar{q}}/\partial p$ Anomalies (W/m^2) JFM 1998 NSIPP



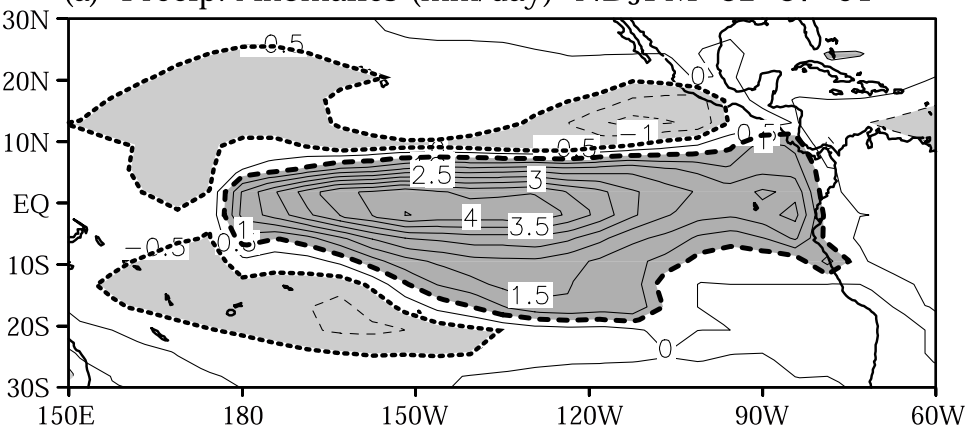
(c) $-\langle\bar{v}\cdot\nabla\bar{q}\rangle - \langle\nabla\cdot\bar{v}q'\rangle$ Anomalies (W/m^2) JFM 1998 NSIPP



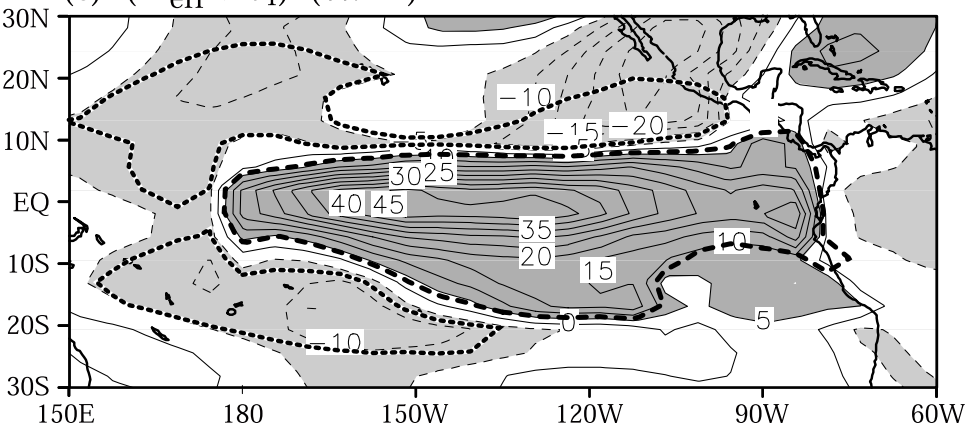
(d) E Anomalies (W/m^2) JFM 1998 NSIPP



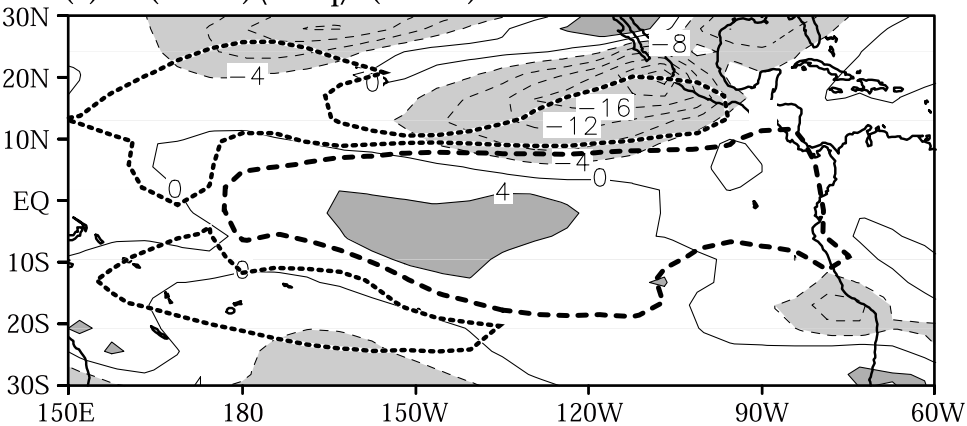
(a) Precip. Anomalies (mm/day) NDJFM '82 '87 '91



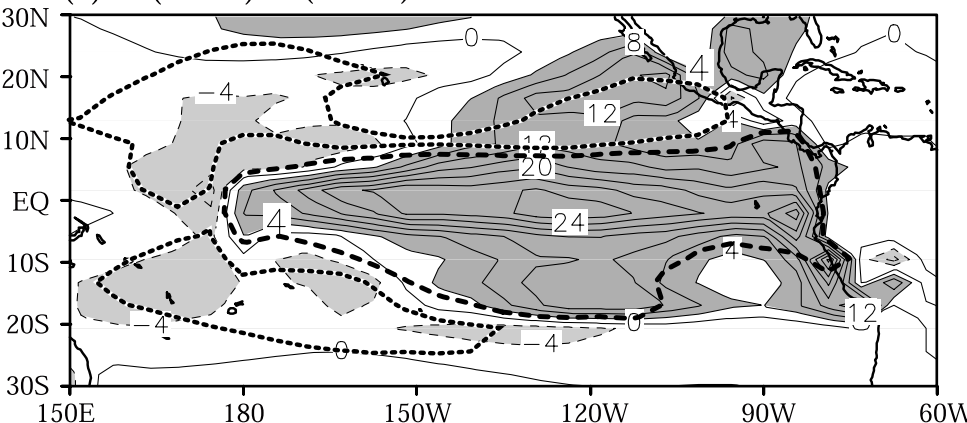
(b) $(M_{\text{eff}} \nabla \cdot \mathbf{v}_1)'$ (W/m^2)



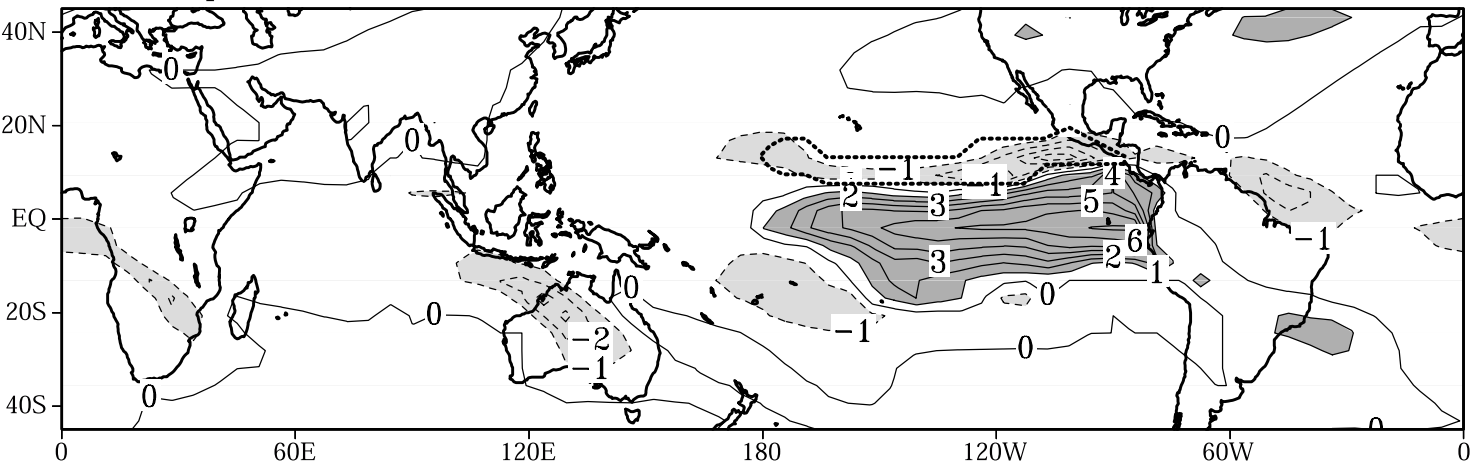
(c) $-(1 + C)\langle \mathbf{v} \cdot \nabla q \rangle'$ (W/m^2)



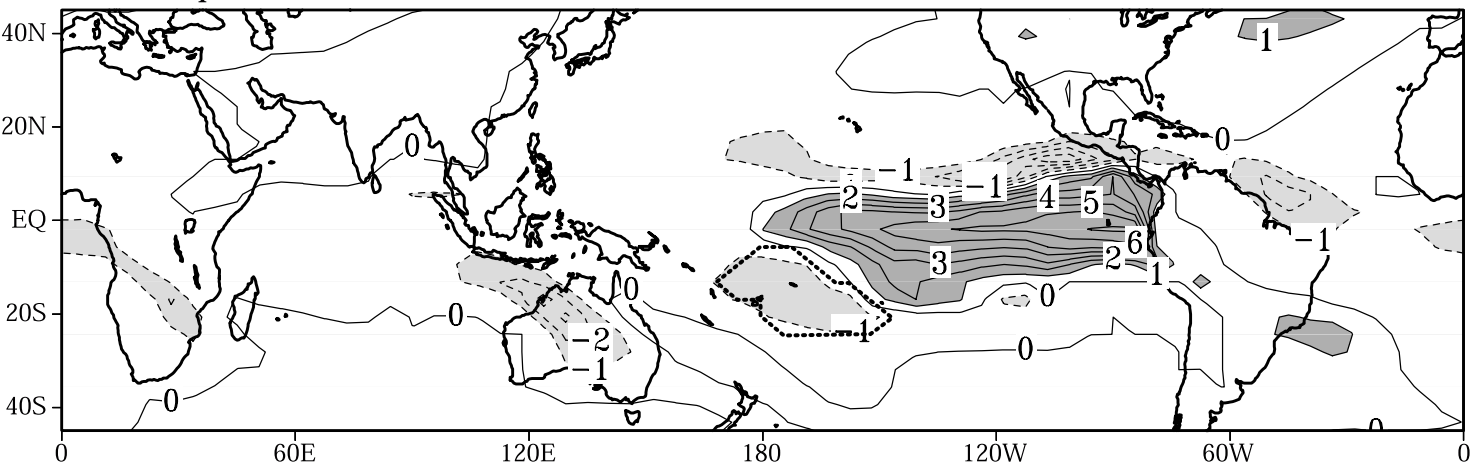
(d) $-(1 + C)E'$ (W/m^2)



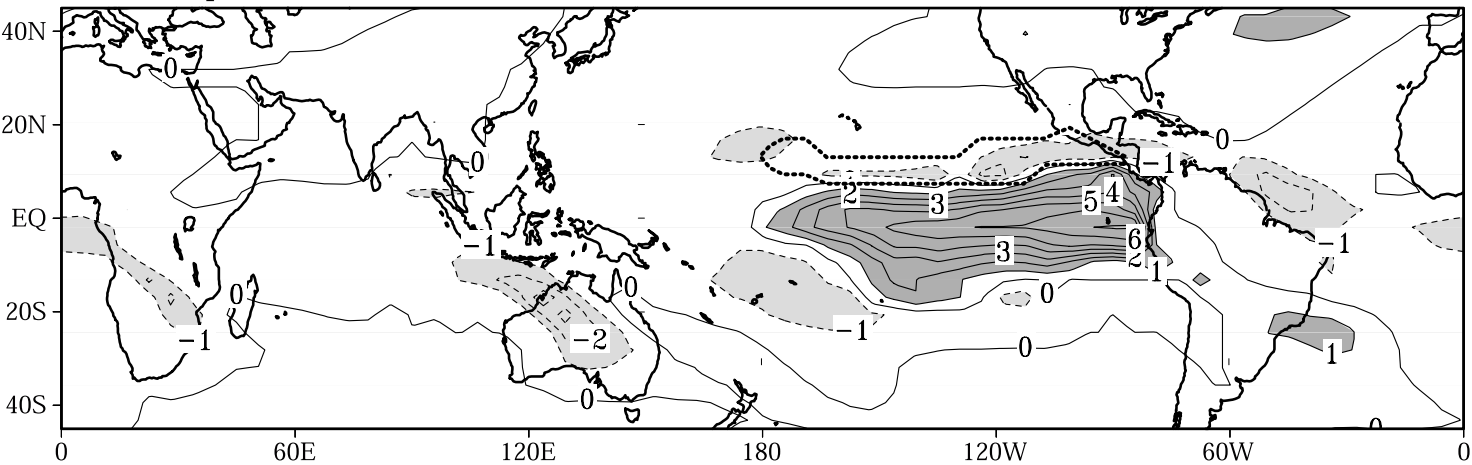
(a) Precip. JFM 1998 CLIMRAD. NORTH - CLIM



(b) Precip. JFM 1998 CLIMRAD. SOUTH- CLIM



(a) Precip. JFM 1998 ADV. NORTH - CLIM



(b) Precip. JFM 1998 SFLUX. SOUTH - CLIM

